C.N.R.S.
Centre National de la Recherche Scientifique

I.N.F.N.
Instituto Nazionale di Fisica Nucleare

Analysis of the sensitivity of the recycled interferometer during C5, C6 and C7 runs.

R. Flaminio, R. Gouaty, E. Tournefier

VIR-NOT-LAP-1390-313

Issue 1
Date: 15th January 2006

VIRGO * A joint CNRS-INFN Project
Project office: Traversa H di via Macerata - I-56021 S. Stefano a Macerata, Cascina (PI)
Secretariat: Telephone (39) 50 752 521 – Fax (39) 50 752 550 – e-mail virgo@pisa.infn.it

Contents

1 Introduction

The recycled configuration is obtained when all the longitudinal degrees of freedom of the Virgo interferometer are controlled. The two Fabry Perot cavities are kept resonant for the carrier component of the laser and the recycling cavity is kept resonant for both the carrier and the sidebands. Moreover the interferometer is locked on the dark fringe. The recycling technique allows the increase of the effective power circulating in the interferometer, which reduces the impact in sensitivity of the photodiode shot noise. The recycled configuration was first tested for 24 hours during the C5 commissioning run in December 2004. It was followed by several technical upgrades which lead to some improvements of the stability and of the sensitivity of the interferometer. Then the C6 run allowed the collection of a two weeks long set of data in the recycled configuration in August 2005. The C7 run was performed one month later in order to test some extra technical upgrades.

The goal of this note is to present the sources of noise which limited the sensitivity during these runs. The run conditions are described in section 2 as well as the sensitivity curves obtained during the C5, C6 and C7 runs. The impact of the recycling technique on the behavior of the common mode rejection factor (CMRF) is discussed in section 3. The noise sources limiting the C5, C6 and C7 runs are described in sections 4, 5 and 6 respectively.

2 The C5, C6 and C7 commissioning runs

During the commissioning of the recycled interferometer it was necessary to reduce the power entering into the interferometer by a factor 10 (0.8 Watts instead of 8 Watts used in the recombined configuration). This modification was necessary since it was found that when the PR mirror is aligned a tiny amount of light is retrodiffused by the input mode cleaner back into the interferometer creating interference fringes which prevented the lock of the interferometer. After the attenuation of the beam between the input mode cleaner and the PR mirror these fringes were well enough reduced so that it was possible to lock the recycled interferometer. The C5 run took place few months after this modification. Its first part was dedicated to the recombined configuration and is described in [1], while the recycled configuration was tested on December 6th and 7th 2004. The C6 run took place 8 months later from July 29^{th} to August 12^{th} 2005 and the C7 run was performed just before the autumn 2005 shutdown, from September 14^{th} to September 19^{th}.

The locking scheme implemented in the recycled configuration for these runs is shown in Figure 1. In addition to the three longitudinal degrees of freedom that have already to be controlled in the recombined configuration (the Fabry-Perot differential mode, the short Michelson differential mode and the Fabry Perot common mode which are defined in [1]), it is also needed to control the length of the recycling cavity in order to keep it resonant. The locking strategy chosen for the recycled configuration is the same for these three runs:

- The Fabry Perot differential mode is controlled with the dark fringe signal ($B1\_ACp$).

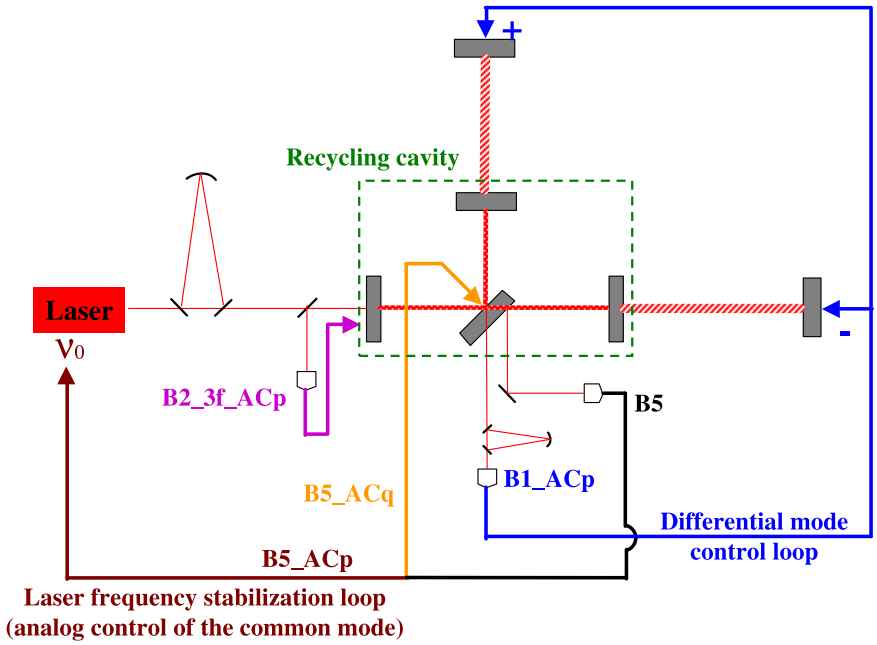

Figure 1: *The recycled locking scheme (for legibility reasons the intput mode cleaner control loops have been omitted).*

- The differential mode of the short Michelson is controlled by acting on the beam splitter mirror. The error signal ($B5\_ACq$) is provided by the photodiode which receives the beam reflected by the anti-reflective side of the beam splitter (B5).
- The Fabry Perot common mode is compensated by adjusting the laser frequency with an analog control loop which uses the other quadrature of B5 ($B5\_ACp$) as error signal.
- The length of the recycling cavity is controlled by acting on the power recycling mirror. The error signal is provided by the signal of the photodiode receiving the beam reflected by the interferometer (B2) demodulated at 3 times the modulation frequency ($B2\_3f\_ACp$).

The angular controls have been improved between the runs. The mirror angular degrees of freedom were locally controlled during the C5 run while during C6 the linear alignment was partially implemented as follows:

- For the west end, west input, north input and power recycling mirrors, the lower frequency part of the angular corrections (below 10 mHz) was provided by a simplified version of the linear alignment, called the drift control, whereas local controls were used for higher frequencies.
- The north end mirror was fully under linear alignment.

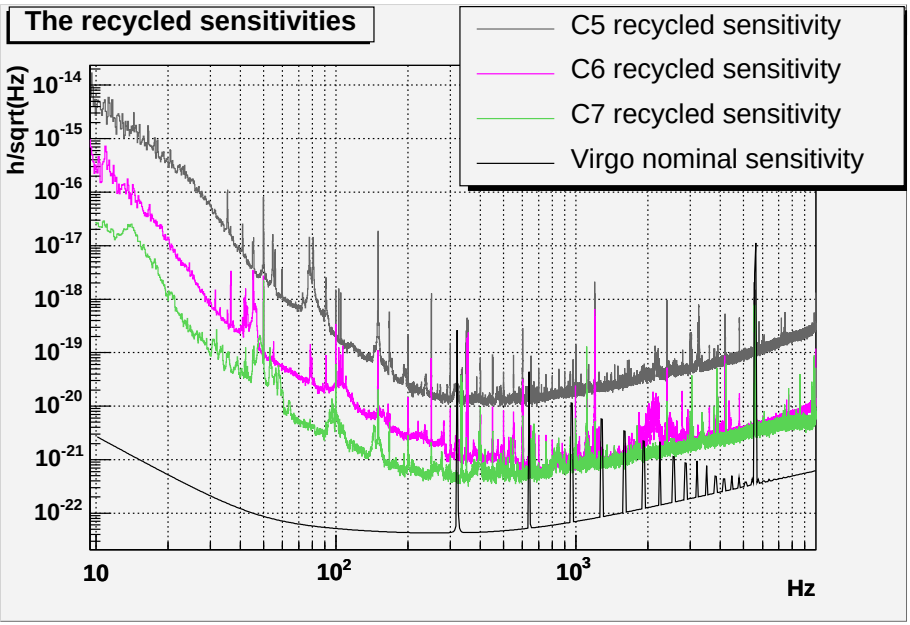

Figure 2: *The recycled sensitivities (C5, C6 and C7 runs).*

- The beam splitter was still under local controls.

During the C7 run the linear alignment was implemented on all the mirrors except the west input mirror which was locally controlled.

Moreover, during the C7 run, the hierarchical control was implemented on the end mirrors suspension. This technique consists in splitting the locking correction signals between the marionette and the reference mass. The low frequency correction forces are applied to the marionette while the high frequency correction forces are applied directly to the mirror. The crossover between these two actuation methods is around 5 Hz.

The sensitivities obtained during the C5, C6 and C7 runs are shown in Figure 2. The noise sources which contribute to these sensitivities are detailled in sections 4, 5 and 6 respectively.

3 The interferometer common mode rejection factor

For an ideal interferometer locked on the dark fringe, the common mode noise is cancelled by the destructive interference between the two arms reflected beams. In practice this cancellation is not perfect due to the presence of asymmetries between the two Fabry Perot cavities like difference of finesse or difference of losses. The Common Mode Rejection Factor (CMRF) quantifies how much a common mode noise (for example a laser frequency noise) is reduced by the effect of the interference process. The CMRF can be defined with the relation:

$$CMRF \;=\; \left|\left|\frac{\delta\tilde{l}/L}{\delta\tilde{\nu}/\nu}\right|\right| \qquad (1)$$

where L is the Fabry Perot cavity length, ν is the laser frequency, $\delta\tilde{l}$[1] refers to the difference of length between the two Fabry Perot cavities which is equivalent for the interferometer output port to the effect of the laser frequency noise $\delta\tilde{\nu}$.
A simulation study using SIESTA [2] has been performed in order to examine the CMRF behavior in the recycled configuration. The results are presented in the following sections. The effect of an asymmetry of the finesses and the effect of an asymmetry of losses are first considered independly in 3.1 and 3.2. The effect of a coupling between these two asymmetries is discussed in 3.3.
The locking control loops are not included in this simulation. An analysis performed in the recombined configuration has shown that even if the control loops can have an impact on the CMRF below a few hundred Hertz, the general trend of the CMRF mainly depends on the optical asymmetries. Moreover due to the very high gain of the laser frequency stabilization loop at low frequency the CMRF is not an issue at these frequencies.

3.1 Impact of an asymmetry of the finesses

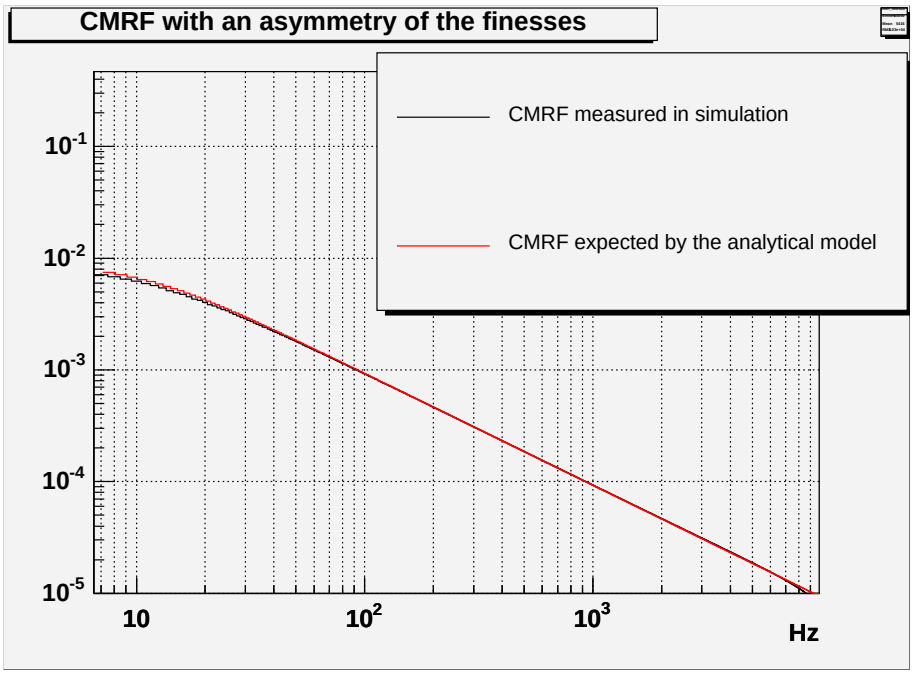

Figure 3: *CMRF due to a finesse asymmetry of* 0.9 %.

As it has been demonstrated in [1] the CMRF resulting from an asymmetry of the finesses between the two Fabry Perot cavities is given in the recombined configuration by:

$$CMRF = \frac{|F_N - F_W|}{F} \frac{1}{\sqrt{1 + \left(\frac{f}{f_{cav}}\right)^2}} \quad (2)$$

[1]Throughout this note the notation $\delta\tilde{X}$ refers to the fluctuation of the variable X taken in the frequency domain, while the notation δX refers to the modulus of $\delta\tilde{X}$.

where F_N and F_W are the finesses of the north and west cavities respectively, and F is the averaged finesse. f_{cav} is the Fabry Perot cavity pole given by the relation: $f_{cav} = \frac{c}{4FL}$. The finesse of each Fabry Perot depends on the reflectivity[2] of the input mirror (r_1) and the reflectivity of the end mirror (r_2) according to the relation:

$$F = \frac{\pi\sqrt{r_1 r_2}}{1 - r_1 r_2} \tag{3}$$

An analytical computation made in [3] shows that the CMRF due to an asymmetry of the finesses in the recycled configuration can be deduced from 3 by replacing the Fabry-Perot cavity pole by the pole of the double cavity f_{recy} since the phase response of the interferometer to a common mode noise is filtered by the double cavity in this configuration:

$$CMRF = \frac{|F_N - F_W|}{F} \frac{1}{\sqrt{1 + \left(\frac{f}{f_{recy}}\right)^2}} \tag{4}$$

whith:

$$f_{recy} = f_{cav} \frac{1 - r_{PR} \cdot \rho_{FP}}{1 + r_{PR}} \tag{5}$$

In relation (5) r_{PR} is the reflectivity of the power recycling mirror (according to a measurement performed by the LMA: $r_{PR}^2 = 92.2\%$, and ρ_{FP} is the averaged reflectivity modulus of the two Fabry Perot cavities. For a resonant cavity ρ_{FP} is given by:

$$\rho_{FP} = \left| \frac{r_1 - (1 - P_1) r_2}{1 - r_1 r_2} \right| \tag{6}$$

where P_1 refers to the input mirror losses.

A simulation of the recycled interferometer has been performed in order to check the analytical model given by equation (4). The values of the main parameters used in this simulation are given in Table 1. An asymmetry of the finesses of 0.9 % has been included by choosing different values for the reflectivities of the two input mirrors. The mirror losses have been set to zero so that the difference between the reflectivity modulus is negligible with respect to the asymmetry of the finesses. The CMRF obtained in simulation is compared to the CMRF given by the analytical model in Figure 3. The two curves are in a good agreement for all the Virgo bandwidth.
This analysis shows that the impact of an asymmetry of the finesses on the CMRF is reduced in the recycled configuration with respect to the recombined configuration, due to the double cavity low-pass filtering which has a significant effect for frequencies above f_{recy}. The maximum finesse asymmetry expected for the real interferometer is about 5 %. This value is obtained by taking into account the Fabry-Perot effect in the input mirrors as explained in [1]. Consequently the maximum value of the CMRF that can result from an asymmetry of the finesses is around 5×10^{-2} at low frequencies (below 10 Hz) and is lower than 5×10^{-4} for frequencies above 1 kHz.

[2]In this note the mirror reflectivities refer to field reflectivities with the notation r and the loss coefficients are expressed in terms of power with the notation P.

Cavity	r_1	r_2	F	f_{cav} (Hz)	f_{recy} (Hz)
North	0.93913	0.99998	50.00	500	10.4
West	0.93967	0.99998	50.46	495	

Table 1: *Values used in the simulation of a finesse asymmetry of* 0.9 %.

3.2 Impact of an asymmetry of the losses

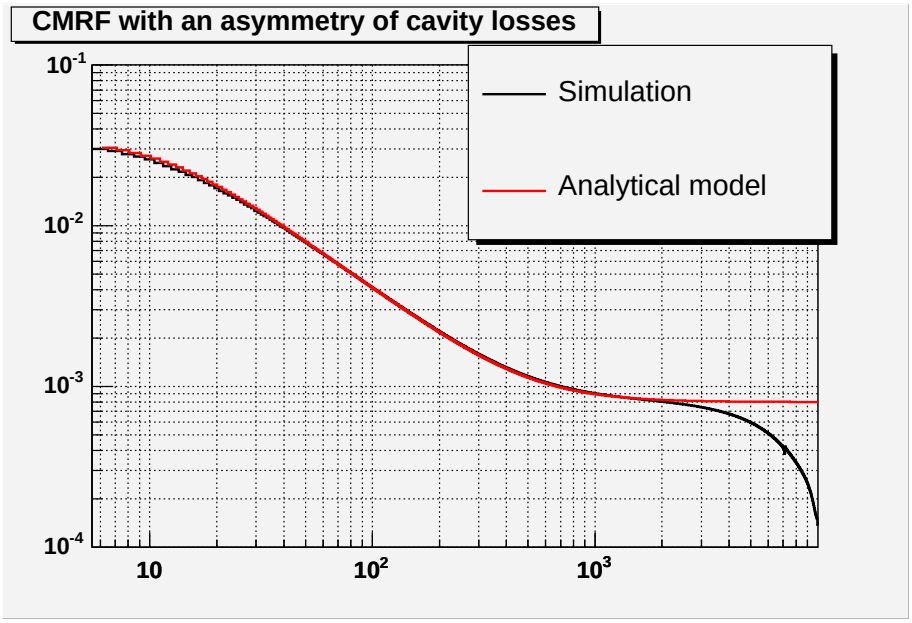

Figure 4: *CMRF due to an asymmetry of losses of 100 ppm.*

In this section the effect of an asymmetry of the losses between the two Fabry Perot cavities is considered, whereas the finesse is supposed to be the same for both arms. In the case of the recombined interferometer the CMRF due to an asymmetry of losses is given by [1]:

$$CMRF_{recomb} = \frac{F}{2\pi}|P_W - P_N| \tag{7}$$

where $P_{N(W)}$ is the round trip losses of the north (west) cavity. A computation made in [3] shows that the CMRF obtained in the recycled configuration is:

$$CMRF = \frac{F}{2\pi}|P_W - P_N| \frac{f_{cav}}{f_{recy}} \frac{\sqrt{1+\left(\frac{f}{f_{cav}}\right)^2}}{\sqrt{1+\left(\frac{f}{f_{recy}}\right)^2}} \tag{8}$$

By comparing equations (7) and (8) one can notice the following differences between the recombined and the recycled configurations:

- At low frequency (below f_{recy}), the CMRF is worsened by a factor equal to $\frac{f_{cav}}{f_{recy}}$, i.e. roughly equal to the recycling gain, which means that the effect of an asymmetry of losses is emphasized by the recycling technique.

- For frequencies higher than the Fabry Perot cavity pole f_{cav}, the amplification effect due to the recycling technique is fully cancelled, and the CMRF flattens. The value of the CMRF at high frequency is the same one as that obtained in the recombined configuration.

The analytical model given in equation (8) has been checked by a simulation study. The values of the optical parameters choosen for this simulation are listed in Table 2.An asymmetry of the round trip losses of 100 ppm inside the cavities has been set. This is a realistic value as shown by a simulation analysis presented in [5], which uses the maps of the mirror substrates and the maps of the mirror coatings measured at the LMA. Figure 4 shows that the CMRF measured in simulation and the CMRF given by the analytical model are in a good agreement. At high frequencies the value of the CMRF drops in the simulation while it is expected to remain constant by the analytical model. This behaviour is not understood but an artefact in the simulation is suspected.

Cavity	r_1	r_2	F	f_{cav} (Hz)	P_1	ρ_{FP}	f_{recy} (Hz)
North	0.9394	0.99998	50.25	497.5	0.4×10^{-3}	0.9936	11.8
West	0.9394	0.99998	50.25	497.5	0.3×10^{-3}	0.9952	

Table 2: *Values used in the simulation for an asymmetry of losses of 100 ppm.*

3.3 Coupling between an asymmetry of finesse and an asymmetry of losses

In this section the simultaneous impacts of both a finesse asymmetry and losses asymmetry are considered. An approximated analytical model of the CMRF is obtained by summing linearly the effects of the two kinds of optical asymmetry:

$$CMRF = \left| \frac{F_N - F_W}{F} \frac{1}{\sqrt{1+\left(\frac{f}{f_{recy}}\right)^2}} + \frac{F}{2\pi}(P_W - P_N)\frac{f_{cav}}{f_{recy}} \frac{\sqrt{1+\left(\frac{f}{f_{cav}}\right)^2}}{\sqrt{1+\left(\frac{f}{f_{recy}}\right)^2}} \right| \quad (9)$$

As shown by equation (9) the contributions of the two kinds of asymmetry add up if the differences $F_N - F_W$ and $P_W - P_N$ are both positive or both negative, whereas one can be compensated by the other if these differences have opposite signs.
The analytical model is compared to simulation results in Figure 5. Two situations are considered:

- The quantities $F_N - F_W$ and $P_W - P_N$ have the same sign. The values of the parameters choosen for the simulation are shown in Table 3.

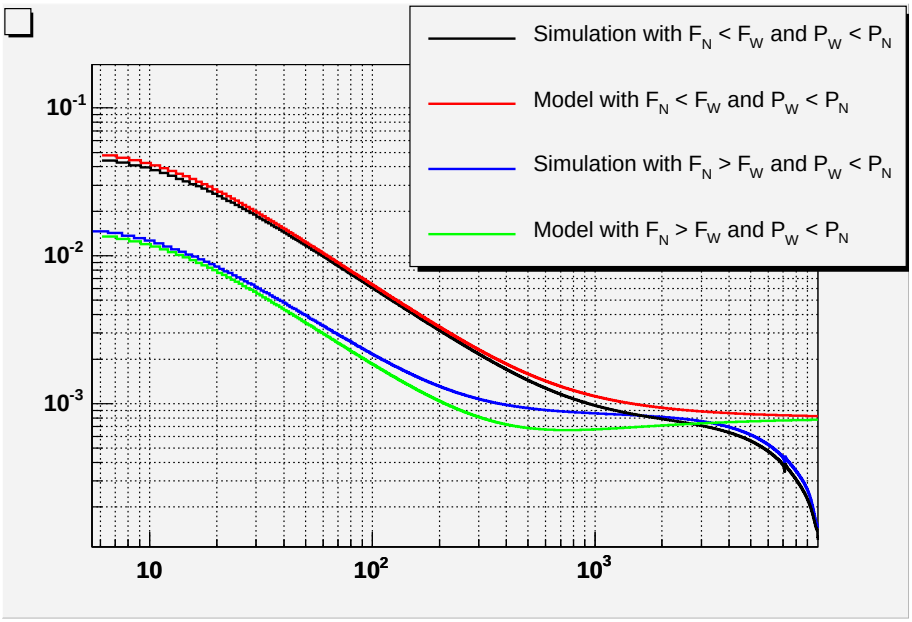

Figure 5: *CMRF due to both finesse asymmetry and an asymmetry of losses.*

- The quantities $F_N - F_W$ and $P_W - P_N$ have opposite sign. The values of the corresponding simulation parameters are shown in Table 4.

In both cases a finesse asymmetry of 2 % and an asymmetry of losses of 100 ppm have been included in the simulation. As it is shown in Figure 5, whatever the signs of the asymmetries are, the CMRF obtained in simulation is in good agreement with the analytical model. At high frequencies (above a few hundred Hertz), the simulation results slightly differ from the analytical model, which must be due to the fact that the model is obtained from a linear approximation. Nevertheless, the model reproduces reasonably well the general behavior of the CMRF.

At high frequencies the CMRF is dominated by the impact of the asymmetry of losses while at low frequency both finesse asymmetry and losses asymmetry can have similar contribution. Therefore the CMRF can be improved at low frequency (below a few hundred Hertz) if the asymmetry of finesse compensates the asymmetry of reflectivity modulus. This condition is satisfied if: $\frac{F_N - F_W}{F} \approx -\frac{F}{2\pi}(P_W - P_N)\frac{f_{cav}}{f_{recy}}$. The asymmetry of finesse can be tuned by using the Fabry Perot effect in the input mirrors, heating one of the mirror.

Cavity	r_1	r_2	F	f_{cav} (Hz)	P_1	ρ_{FP}	f_{recy} (Hz)
North	0.9379	0.99998	49.0	510	0.4×10^{-3}	0.9936	11.8
West	0.9391	0.99998	50.0	500	0.3×10^{-3}	0.9952	

Table 3: *Values used in the simulation of a finesse asymmetry of* 2.0 % *(with* $F_N < F_W$*) combined with an asymmetry of losses of 100 ppm (with* $P_W < P_N$*).*

Cavity	r_1	r_2	F	f_{cav} (Hz)	P_1	ρ_{FP}	f_{recy} (Hz)
North	0.9391	0.99998	50.0	500	0.4×10^{-3}	0.9936	11.8
West	0.9379	0.99998	49.0	510	0.3×10^{-3}	0.9952	

Table 4: *Values used in the simulation of a finesse asymmetry of* 2.0 % *(with* $F_N > F_W$*) combined with an asymmetry of losses of 100 ppm (with* $P_W < P_N$*).*

4 Analysis of the C5 run sensitivity

The results of the analysis of the sensitivity obtained during the C5 run in the recycled configuration are presented in this section. The contributions of the dark fringe readout noises and of the demodulation noise in the high frequency part of the sensitivity (above 400 Hz) are discussed in 4.1 and 4.2 respectively. The impact of the actuator noise (in the intermediate frequency region) is discussed in 4.3. The noises introduced by the control loops, which limit the sensitivity at low frequency (below 100 Hz), are described in 4.4.

4.1 Dark fringe readout noises

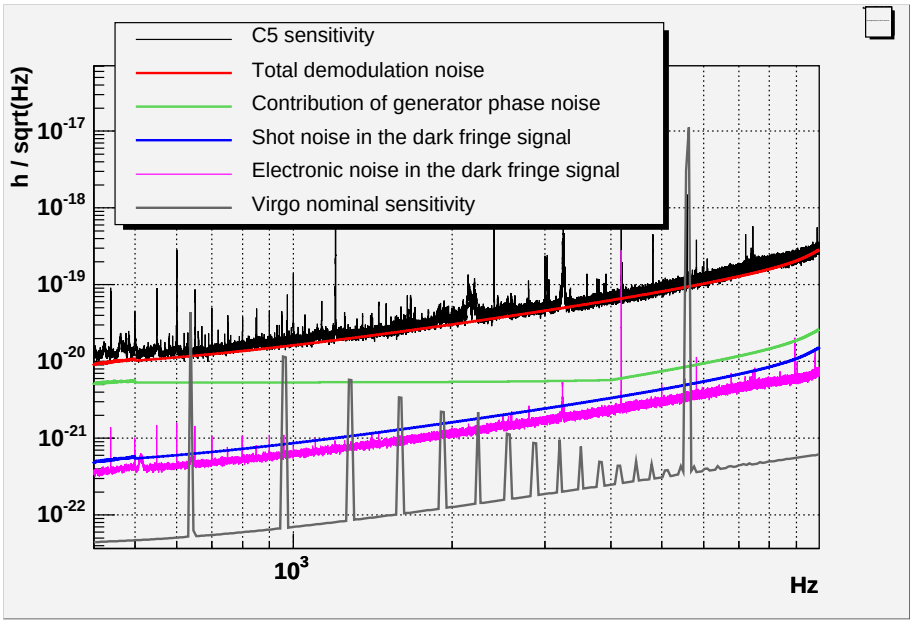

Figure 6: *Noises at high frequency during the C5 run: dark fringe readout noises and demodulation noise.*

The dark fringe readout noises refer to the electronic noise and the shot noise of the B1 photodiodes (which provides the dark fringe signal). The B1 electronic noise is measured with the $B1\_ACp$ channel by closing the shutter on that beam, in order to guarantee that no light reaches the photodiodes. This measurement gives a white noise approximatively equal to $5.5 \times 10^{-11} W/\sqrt{Hz}$. The B1 shot noise is evaluated from the DC power (P_{DC}) which reaches the photodiodes when the interferometer is at its working point (during

the C5 run $P_{DC} \approx 7.6\ mW$). Both electronic and shot noises are then converted in $h/\sqrt{Hz}$ by using the calibration transfer function. The contributions in sensitivity of the B1 shot noise and the B1 electronic noise are shown in Figure 6. They are lower than the sensitivity curve by a factor 20 and a factor 30 respectively. One can conclude that the contribution of the B1 readout noises in the C5 run sensitivity is negligible.

4.2 Demodulation noise

Between 400 Hz and 10 kHz the C5 sensitivity obtained in recycled configuration is actually limited by demodulation noise, as shown here.

4.2.1 Identification and modelization of the demodulation noise

The demodulation noise refers to a phase noise which couples to the dark fringe signal (given by $B1\_ACp$ channel) during the demodulation process, via $B1\_ACq$ channel. As shown in Appendix A, the demodulation noise projected on the dark fringe signal δACp is given by:

$$\delta \tilde{ACp} \ = \ ACq_0 \ \delta\tilde{\phi}_{dem} \tag{10}$$

where $\delta\tilde{\phi}_{dem}$ refers to the relative fluctuation of phase between the interferometer signal and the oscillator signal used for demodulation, and ACq_0 is the mean value of $B1\_ACq$ signal. According to equation (10) the demodulation noise seen in the dark fringe signal ($B1\_ACp$) varies proportionally to the amount of signal in $B1\_ACq$ channel.
The result of an analysis performed on a 200 s long set of data corresponding to a period of the C5 run is shown in Figure 7. In this figure the high frequency noise measured in the dark fringe signal (y axis) is plotted as a function of the mean value of $B1\_ACq$ signal (x axis). The result is compatible with the hypothesis of a relation of proportionality between these two quantities, which tends to prove that the noise limiting the sensitivity at high frequency is demodulation noise. The corresponding level of phase noise $\delta\phi_{dem}$ entering the demodulation board can be deduced from the slope of the straight line which fits to the experimental points in Figure 7, which gives: $\delta\phi_{dem} \approx 0.52\ \mu rad/\sqrt{Hz}$.

The contribution of the demodulation noise to the dark fringe signal is obtained using equation (10). It is then converted into $h/\sqrt{Hz}$ by using the calibration transfer function. The result of this estimation is shown in Figure 6. The curve entitled "Total demodulation noise" has been obtained assuming $\delta\phi_{dem} \approx 0.52\ \mu rad/\sqrt{Hz}$ for all frequencies. In order to estimate the amount of signal in $B1\_ACq$ for the 300 s long set of data used to obtain the sensitivity curve, the mean value of $B1\_ACq$ has been computed for each segment of 0.1 s and then the values obtained with all the segments of data have been averaged quadratically. The averaged mean value corresponds to $ACq_0 = 5.45$ Volts. The demodulation noise obtained with this value explains well the sensitivity curve above 400 Hz.

It is then needed for noise reduction purpose to understand what is the origin of the phase noise $\delta\phi_{dem}$ obtained at the demodulation level. Two different origins for the phase noise $\delta\phi_{dem}$ have been suspected: it can be induced by the intrinsic phase noise of the generator which delivers the oscillator signal used to modulate the phase of the laser, or it can be generated at the level of the detection electronics itself. These two hypothesis

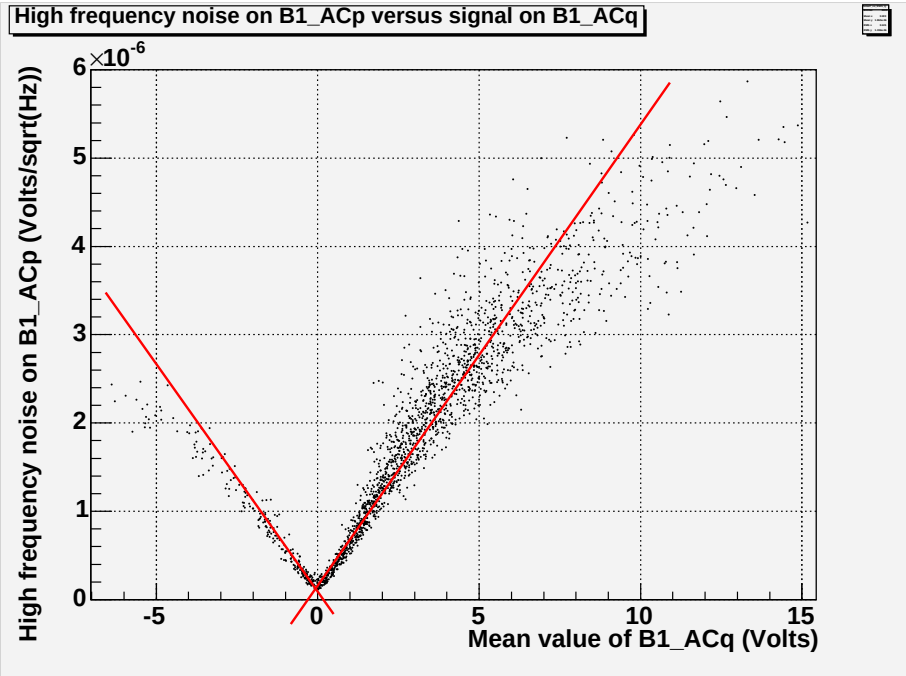

Figure 7: *High frequency noise on B1_ACp (given by the averaged spectrum between 4000 and 5000 Hz) as a function of the mean value of B1_ACq signal. The units are expressed in term of equivalent voltage obtained after the demodulation process and added for the two photodiodes of B1. Each point is computed on 0.1 s of data.*

are examined in the following sections.

4.2.2 Phase noise generated by the signal generator

The intrinsic phase noise of the generator ($\delta\phi_{gen}$) is common to both the laser beam and the oscilator signal used for demodulation. Nevertheless it does not cancel in the demodulation process due to the delay introduced by the input mode cleaner on the interferomter signal. This situation is schematized in Figure 8.
The phase fluctuation $\delta\phi_{ITF}$ of the interferometer signal is given by:

$$\delta\tilde{\phi}_{ITF} \;=\; \delta\tilde{\phi}_{gen}\frac{1}{1+i\frac{f}{f_{IMC}}} \tag{11}$$

Equation (11) shows that before propagating to the interferometer signal the generator phase noise is filtered by the input mode cleaner cavity. The frequency cut-off f_{IMC} is equal to 500 Hz. The effect of the recycling cavity is negligible with respect to the input mode cleaner cavity, and there is no effect due to the Fabry Perot cavities because the sidebands do not resonate inside these cavities.
If one assumes that the delay introduced by the electrical cables which link the generator to the detection electronics is negligible, one can write:

$$\delta\tilde{\phi}_{LO} \;=\; \delta\tilde{\phi}_{gen} \tag{12}$$

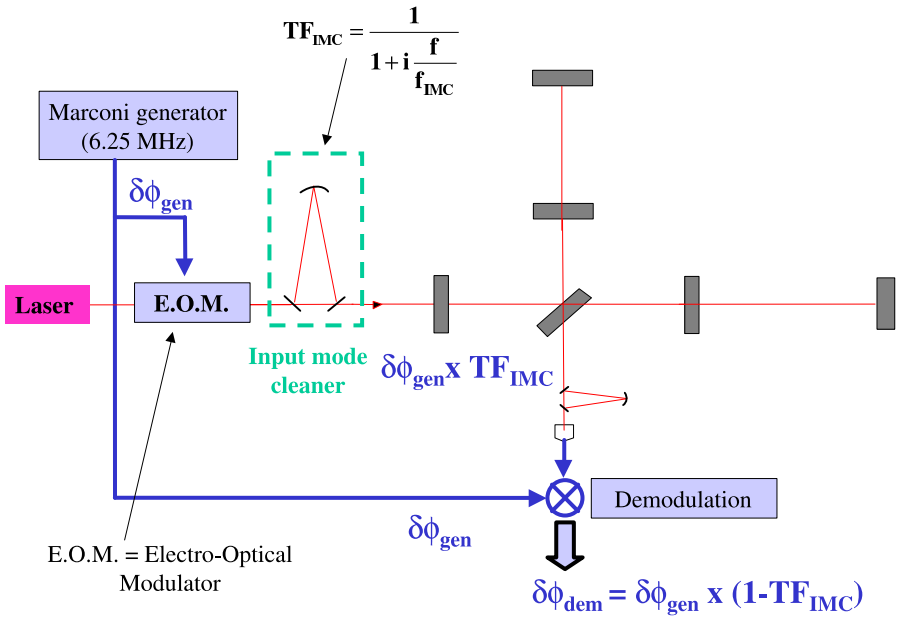

Figure 8: *Propagation scheme of the generator phase noise into the demodulated signal of the interferometer output port.*

where $\delta\phi_{LO}$ is the phase fluctuation of the oscillator signal used for demodulation. Finally the relative fluctuation of phase between the interferometer signal and the local oscillator, referred to as $\delta\phi_{dem}$, is given by:

$$\delta\phi_{dem} = \left|\left|\delta\tilde{\phi}_{LO} - \delta\tilde{\phi}_{ITF}\right|\right| = \delta\phi_{gen}\frac{\frac{f}{f_{IMC}}}{\sqrt{1+\left(\frac{f}{f_{IMC}}\right)^2}} \quad (13)$$

The signal generator is a Marconi 2040 whose specifications (given for a signal frequency of 80 MHz) are:

- For $f < 4000\ Hz$: $\delta\phi_{gen} = \frac{2\times10^{-4}}{f}\ (rad/\sqrt{Hz})$
- For $f > 4000\ Hz$: $\delta\phi_{gen} = 5\times10^{-8}\ (rad/\sqrt{Hz})$

The contribution in sensitivity of the signal generator phase noise can be computed by using relations (13) and (10). The result of this computation is shown in Figure 6. The model of the generator phase noise is lower by a factor ranging between 2 and 10 than the C5 sensitivity curve. Therefore the origin of the phase noise has to be found somewhere else.

4.2.3 Phase noise generated by the local oscillator board

The phase noise can also be generated by the electronics of the detection chain. The main candidate as source of phase noise is the local oscillator board which provides the oscillator signal to the demodulation board.

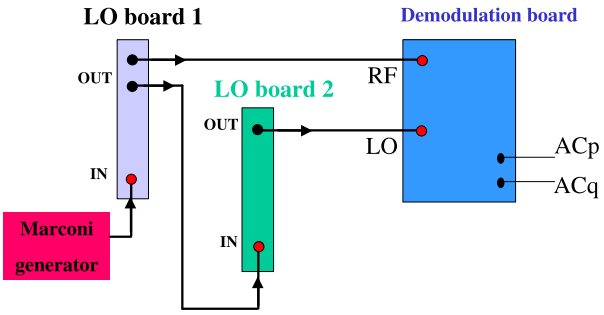

Figure 9: *Simplified electronic scheme used for the measurement of the phase noise generated by the local oscillator board (LO board).*

A measurement of the phase noise generated by the local oscillator board has been performed using the experimental setup shown in Figure 9. The Marconi generator is plugged to a first local oscillator board (LO board 1) which provides as output two identical oscillator signals. One of these signals is directly sent to the RF input of a demodulation board (which usually receives the photodiode signal), and the other passes through another local oscillator board (LO board 2) before being sent to the LO input of the demodulation board. The electronics of the LO board 2 is tuned so that the phase of the signal entering the LO input of the demodulation board is turned by 90° with respect to the signal entering the RF input. In these conditions the demodulation process induces a signal in the ACq channel whereas the ACp channel contains phase noise. As a consequence, by comparing the high frequency noise measured in the ACp channel to the signal value measured in the ACq channel one obtains an estimation of the phase noise generated by the LO board 2 (the phase noise generated by the Marconi generator and the LO board 1 is cancelled by the demodulation process because it is common to both RF and LO inputs). The measurement provides: $\delta\phi_{dem} \approx 0.33\ \mu rad/\sqrt{Hz}$.
In the standard configuration the RF input of the demodulation board receives the interferometer signal whereas the LO input of the demodulation board receives the oscillator signal which has passed through two LO boards. Therefore the expected phase noise is the incoherent sum of the phase noise coming from both LO boards:

$$\delta\phi_{dem} = \sqrt{2} \times 0.33\ \mu rad/\sqrt{Hz} \approx 0.47\ \mu rad/\sqrt{Hz} \tag{14}$$

This result is in agreement with the value of $\delta\phi_{dem}$ deduced from Figure 7.

One can conclude from these results that the C5 recycled sensitivity is mainly limited at high frequency by the demodulation noise induced by the phase noise of the local oscillator boards. This noise couples to the dark fringe signal through the other quadrature of B1 ($B1\_ACq$). It was observed that the amplitude of this signal increases with misalignments of the interferometer. Two kinds of improvements can therefore be planned in order to reduce the contribution in sensitivity of the demodulation noise:

- The coupling of phase noise to the dark fringe can be reduced if the amount of signal in the $B1\_ACq$ channel is reduced. This can be acheived by improving the alignment conditions of the interferometer, as was already observed in the recombined configuration when the linear alignment has been implemented,
- The electronics of the local oscillator boards or the electronics of the generator can be improved in order to reduce the phase noise at its source.

4.3 Actuator noise

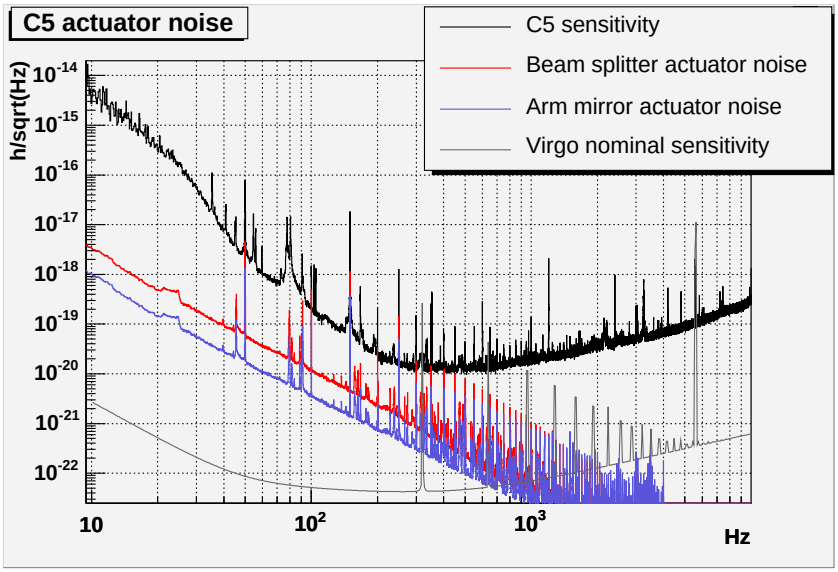

Figure 10: *Actuator noise during the C5 run.*

The actuator noise refers to the electronic noise generated by the Digital Analog Convertor (DAC) and the coil drivers implemented in the mirror actuation chain. The contribution in sensitivity of the mirror actuator noise during the C5 run has already been estimated in [1] for the recombined configuration. As the analytical models used to propagate the actuator noise in the sensitivity are the same for both recombined and recycled configurations, the estimation performed in [1] is used here. This estimation provides the results shown in Figure 10, where the C5 recycled sensitivity is compared to the contribution of the beam splitter actuator noise and to the contribution of the four arm mirrors actuator noise.
As demonstrated in [1], the contribution in sensitivity of the four arm mirrors actuator noise is given by:

$$h \;=\; \left|\left|\frac{1}{L}\sqrt{8}\; k_a.K_{DC}.E.M.\delta\tilde{u}\right|\right| \tag{15}$$

where:

- δu is the averaged actuator noise for every coil, expressed in equivalent DAC output voltage. A measurement performed in January 2005 on the coils of each arm tower, as no signal was sent to the DAC, provided: $\delta u = 440\ nV/\sqrt{Hz}$.

- E and M are respectively the electrical response of the coil and the mechanical response of the mirror. Their expressions can be found in [1].
- $k_a = \frac{R_{coil}}{R_{coil}+R_{serie}}$. k_a is the attenuation factor of the actuator noise obtained when a serial resistor R_{serie} is implemented in the actuation electronics (during the C5 run, in the low noise configuration: $R_{serie} \approx 250\ \Omega$). R_{coil} is the intrinsic resistor of the coil ($R_{coil} \approx 11\ \Omega$).
- K_{DC} has been defined in [1] as the absolute DC conversion factor from DAC output voltage to mirror longitudinal displacement measured whith $R_{serie} = 0$. For the four arm mirrors: $K_{DC} = 6\ \mu m/V$ with an uncertainty of 20%. This value is deduced from the calibration measurements described in [4].
- The factor $\sqrt{8}$ is for the quadratic sum on the eight coils which were plugged in the arm towers during the C5 run.

The contribution in sensitivity of the beam splitter actuator noise is given by:

$$h = \left|\left|\frac{1}{L}\sqrt{4}\sqrt{2}\frac{\pi}{2F}K_{DC}.E.M.\delta\tilde{u}\right|\right| \tag{16}$$

where:

- $K_{DC} = 25\ \mu m/V$. This value has been obtained during the run from a measurement of the amplitudes of the permanent calibration lines on the NE (at 353 Hz), the WE (at 355 Hz) and BS (at 357 Hz). It makes use of the knowledge of the value of K_{DC} for the NE and the WE mirrors as well as the coils cut-off frequency. The uncertainty on these values leads to a precision on K_{DC} of 20%.
- the $\sqrt{2}$ takes into account the fact that the Beam Splitter mirror is at 45 degrees with respect to the beam.
- $\sqrt{4}$ is for the quadratic sum on the four coils plugged in the beam splitter tower.
- $\frac{\pi}{2F}$ is the inverse of the number of round-trips made by the carrier in the resonant cavity.
- δu is assumed to be at the same value as that measured on the arm towers.

For what concerns the beam splitter mirror the low noise configuration was not implemented during the C5 run ($R_{serie} = 0$). This is the reason why the contribution of the beam splitter actuator noise is higher by a factor 3 than the total contribution of all the other mirrors, as it shown in Figure 10. According to this estimation the actuator noise is at least one order of magnitude lower than the sensitivity curve for the full Virgo bandwidth. Nevertheless it must be mentionned that the analysis of the C6 run indicates that an additional non linear noise can be present when a correction signal is sent to the DAC (see 5.3.1). As a consequence the actuator noise estimations shown in Figure 10 could be underestimated.

4.4 Noise introduced by the control loops

The noise limiting the C5 sensitivity between 10 and 100 Hz is introduced by control loops as shown in this section. These control loops have been identified with coherence computation as it is discussed in 4.4.1. The control noises of the beam splitter explain the major part of the sensitivity curve in this region of frequencies as it is confirmed by the analytical models presented in 4.4.2.

4.4.1 Identification of the mirror control noises

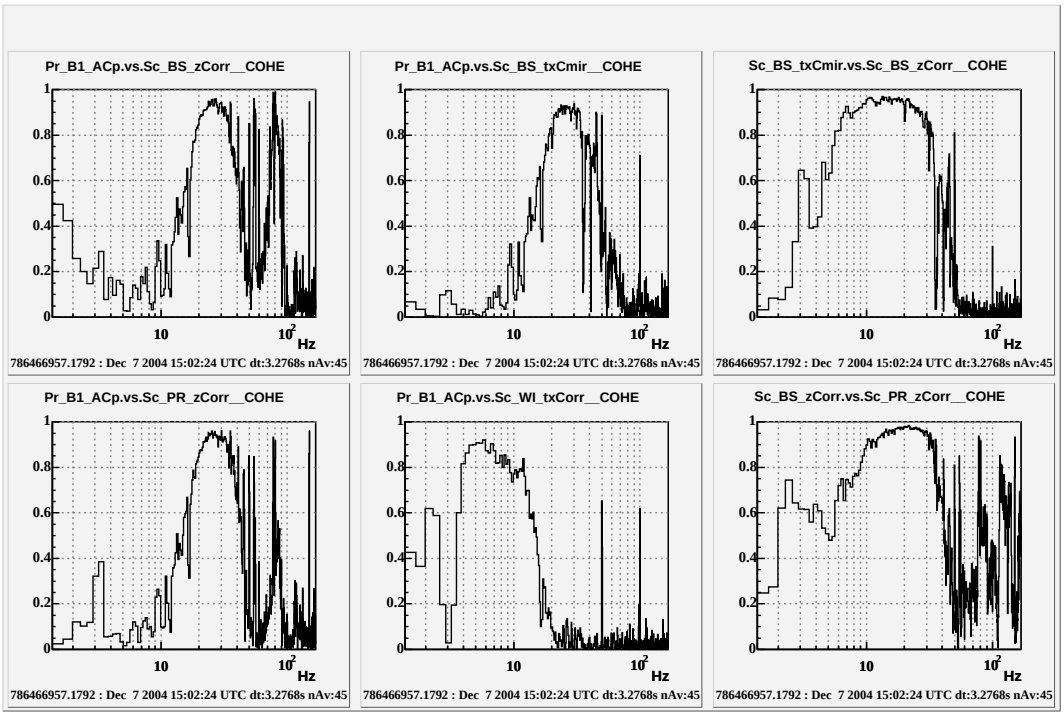

Figure 11: *Coherence functions obtained in recycled configuration during the C5 run in the 10-100 Hz region: between the dark fringe signal and correction signals (left and middle plots), between the beam splitter longitudinal correction signal and other correction signals (right plots).*

As shown in Figure 11, significant coherence has been found between the dark fringe signal and four different correction signals:

- the longitudinal correction signal of the beam splitter mirror (top left plot);
- the angular correction signal sent to the beam splitter mirror actuators to control the θ_x degree of freedom (top middle plot); θ_x refers to the rotation of the mirror around its horizontal axis;
- the longitudinal correction signal of the power recycling mirror (bottom left plot);
- the angular correction signal sent to the marionette actuator of the west input mirror to control the θ_x degree of freedom (bottom middle plot).

In the lowest frequency region of the Virgo bandwidth (around 10 Hz) the dark fringe signal is only coherent with the west input (WI) θ_x angular correction signal. The value of the coherence function (around 80 %) indicates that the sensitivity is mainly limited by the noise introduced by the WI θ_x angular control in this region of frequencies. As mentionned in 2, the linear alignment was not yet implemented in the recycled configuration during the C5 run: all the mirrors were under local controls which are noisier and less efficient than the linear alignment strategy.

From 15 Hz to 100 Hz some coherence (which reaches a level of 90 % in the 20-35 Hz region) is visible between the dark fringe signal and three different correction signals simultaneously, so that it is not possible to directly identify the control loop which is effectively responsible for the introduction of noise in this frequency region. Moreover, as shown in the right plots of Figure 11, three correction signals (beam splitter longitudinal control, beam splitter θ_x angular control, and recycling mirror longitudinal control) are also coherent between each other, which indicates a coupling between the corresponding degrees of freedom. Consequently, as in [1] a cross-coherence computation has been performed in order to better identified the control loops responsible for the noise introduction. This computation is explained in the following.

The noise entering the dark fringe signal (denoted as X_0) is assumed to be composed of four contributions:

$$X_0 \;=\; aX_1 \;+\; bX_2 \;+\; cX_3 \;+\; dX_4 \tag{17}$$

where X_1, X_2, X_3 refers respectively to the beam splitter longitudinal correction signal, the beam splitter θ_x angular correction signal, the recycling mirror longitudinal correction signal, and X_4 is the possible remaining noise which is supposed to be incoherent with the three previous signals. X_0, X_1, X_2, X_3 and X_4 are normalized by their amplitude spectrum modulus (for example $X_0 \;=\; \frac{B1\_\tilde{A}Cp}{||B1\_\tilde{A}Cp||}$, where $B1\_\tilde{A}Cp$ is the amplitude spectrum of the dark fringe signal) so that the coherence function defines a scalar product between these elements. The complex transfer functions a, b and c are obtained by solving the following system:

$$\left\{\begin{array}{l} < X_1, X_0 > = a \;+\; b < X_1, X_2 > \;+ c < X_1, X_3 > \\ < X_2, X_0 > = a < X_2, X_1 > \;+ b \;+\; c < X_2, X_3 > \\ < X_3, X_0 > = a < X_3, X_1 > \;+ b < X_3, X_2 > \;+ c \end{array}\right. \tag{18}$$

where the notation $< X, Y >$ refers to the complex coherence between the variables X and Y.

The total contribution in the dark fringe signal of all control noises (δn_{total}) is given by:

$$\begin{array}{rl} \delta n_{total} \;=\; B1\_ACp & \Big(||a||^2 + ||b||^2 + ||c||^2 + 2Re(\bar{a}b < X_1, X_2 >) \\ & +2Re(\bar{a}c < X_1, X_3 >) + 2Re(\bar{c}b < X_3, X_2 >)\Big)^{\frac{1}{2}} \end{array} \tag{19}$$

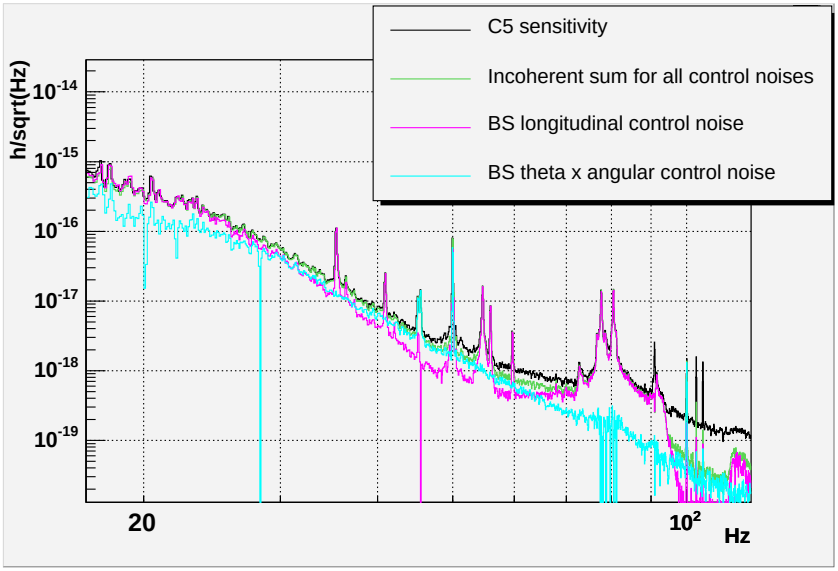

Figure 12: *Contribution of the beam splitter (BS) control noises in the C5 sensitivity. These estimations have been obtained with the cross-coherence computation.*

The incoherent sum δn_{total} can be splitted into three contributions:

$$\delta n_{BS,z} = B1\_ACp \left(||a||^2 + Re(\bar{a}b < X_1, X_2 >) + Re(\bar{a}c < X_1, X_3 >) \right)^{\frac{1}{2}} \quad (20)$$

$$\delta n_{BS,tx} = B1\_ACp \left(||b||^2 + Re(\bar{a}b < X_1, X_2 >) + Re(\bar{c}b < X_3, X_2 >) \right)^{\frac{1}{2}} \quad (21)$$

$$\delta n_{PR,z} = B1\_ACp \left(||c||^2 + Re(\bar{a}c < X_1, X_3 >) + Re(\bar{c}b < X_3, X_2 >) \right)^{\frac{1}{2}} \quad (22)$$

$\delta n_{BS,z}$ and $\delta n_{BS,tx}$ are respectively the contributions of the beam splitter longitudinal control noise and the beam splitter angular control noise, to the dark fringe signal. $Re(\bar{a}b < X_1, X_2 >)$, $Re(\bar{a}c < X_1, X_3 >)$ and $Re(\bar{c}b < X_3, X_2 >)$ are corrective terms which take into account the coupling effects between the different degrees of freedom.
The estimation of equation (22) shows that the contribution of the power recycling mirror longitudinal control noise ($\delta n_{PR,z}$) is negligible. This means that the coherence observed in Figure 11 between the corresponding correction signal and $B1\_ACp$ is not relevant. This can be interpreted by noticing that a longitudinal displacement δL_{BS} of the beam splitter mirror induces a variation of the recycling cavity length δl_{recy}, given by:

$$\delta l_{recy} = \frac{\sqrt{2}}{2} \delta L_{BS} \quad (23)$$

As a consequence, the beam splitter longitudinal control noise, which is seen by the dark fringe signal, also couples to the error signal of the power recycling longitudinal control loop. This mechanism can explain the coherence observed between the power recycling correction signal and $B1\_ACp$, as well as the coherence observed between the power recycling and the beam splitter correction signals (bottom right plot of Figure 11).

The contributions in sensitivity of the beam splitter longitudinal control noise ($\delta n_{BS,z}$), the beam splitter angular control noise ($\delta n_{BS,tx}$), and their incoherent sum (δn_{total}) are shown in Figure 12. According to the cross-coherence computation, the beam splitter control noises explain the major part of the sensitivity curve in the 15-94 Hz range. The beam splitter θ_x angular control noise has a dominant impact between 42 and 53 Hz, whereas the impact of the beam splitter longitudinal control noise seems to prevail around 20 Hz and in the regions where complex structures are visible (around 35 Hz, 41 Hz, between 54 and 60 Hz, and between 70 and 94 Hz).

In order to understand how these noises propagate to the dark fringe signal some analytical models have been developped. To this purpose the analytical models presented in [1] for the recombined configuration can also be applied to the recycled configuration and are used in the following.

4.4.2 Analytical model for the propagation of BS angular control noise

The model associated to the beam splitter θ_x angular control noise is obtained by assuming that the incident beam is vertically miscentered with respect to the beam splitter mirror (as in [1]):

$$h \;=\; \Big|\Big|\frac{1}{L}\; 2\; d\; \frac{\pi}{2F}\; K^{\star}_{DC,\theta_x}.E.M_{\theta_x}.\tilde{BStxCmir}\Big|\Big| \tag{24}$$

where BStxCmir is the spectrum of the correction signal sent to the mirror actuators to control the θ_x angular position of the beam splitter, M_{θ_x} is the mechanical response of the mirror (given by a second order low pass filter with a double pole at 3.3 Hz), $K^{\star}_{DC,\theta_x}$ is the angular actuation gain between the correction signal and the effective mirror rotation ($K^{\star}_{DC,\theta_x} \;\approx\; 45\; \mu rad/V$), and d is the vertical miscentering. The result shown in Figure 13 is obtained by assuming d = 1.55 cm in order to adjust the model to the sensitivity curve in the region around 45 Hz where the coherence with $B1\_ACp$ is maximum. This value of miscentering is in a perfect agreement with the value deduced from the analysis of the recombined sensitivities of C4 and C5 runs [1]. The projection of the beam splitter θ_x angular control noise shown in Figure 13 is in a good agreement with the prediction given by the cross-coherence computation, except in the region around 30 Hz where the model gives a result lower by 60 % than the estimation obtained from coherence functions.

4.4.3 Analytical model for the propagation of BS longitudinal control noise

The model associated to the beam splitter longitudinal control noise is given by ([1]):

$$h \;=\; \Big|\Big|\frac{1}{L}\sqrt{2}\frac{\pi}{2F}2K_{DC}.E.M.\tilde{BSzCorr}\Big|\Big| \tag{25}$$

where BSzCorr is the spectrum of the correction signal sent to the beam splitter actuators. The projection obtained with this model is shown in Figure 13.
The model reproduces well the shape of the noise structures visible in the sensitivity curve between 35 and 94 Hz but their predicted amplitude is 20 % lower than the measured

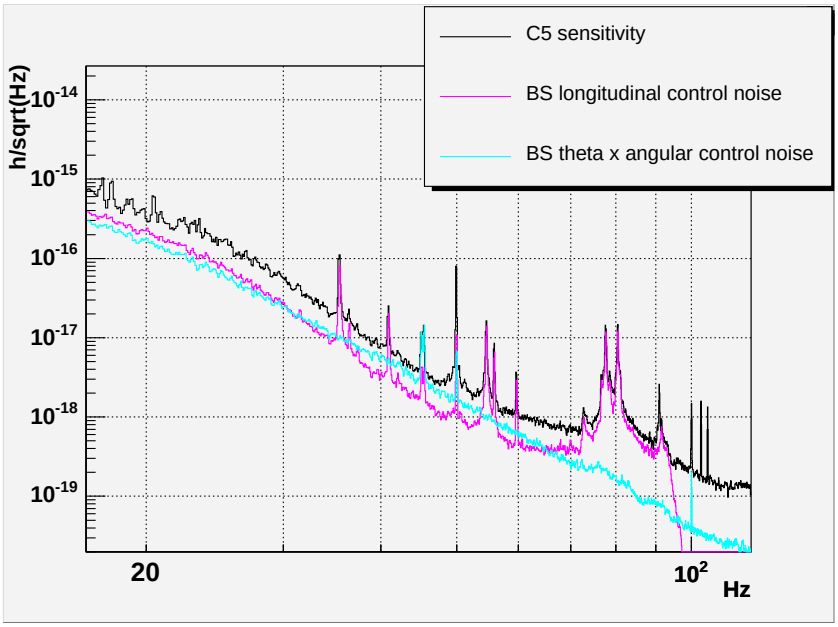

Figure 13: *Beam splitter (BS) control noises estimated with analytical models. The beam splitter θ_x angular control noise is projected on the dark fringe signal assuming a miscentering of 1.55 cm.*

sensitivity. This is nevertheless compatible with the uncertainty of the model since K_{DC} is known only within 20 % (see section 4.3). Moreover, as explained in [4] the sensitivity curve could be overstimated by 20%. Therefore the model of the beam splitter longitudinal control noise is able to explain explain the complex structures found between 35 and 94 Hz, as it has been predicted by the cross-coherence computation. These structures have been identified as input bench mechanical resonances. The mechanism which explains how these resonances couple to the error signal of the beam splitter longitudinal control loop can be found in section 4.4.3 of [1].
Concerning the region around 20 Hz, the model does not fully reproduce the measured sensitivity curve, as expected by the result of the cross-coherence computation. However the accuracy on the sensitivity measurement is likely to be worsened for frequencies lower than 30 Hz, so that the error margin could be underestimated. Despite the difference between the model and the cross-coherence computation, one can nevertheless assert that the beam splitter longitudinal control noise is one of the main sources of noise around 20 Hz.

It can be noticed that the peak at 45 Hz visible in the sensitivity curve and explained by the beam splitter angular control noise is also visible in the spectrum of the beam splitter longitudinal correction signal. This means that the angular noise also couples to the error signal of the beam splitter longitudinal control loop ($B5\_ACq$). This hypothesis is also supported by the high coherence, from 5 to 40 Hz, between the longitudinal and angular error signals of the beam splitter, as shown on Figure 11. This can be explained by the fact that if the beam is miscentered on the BS mirror any rotation of this mirror induces a change in the differential length of the small Michelson and is therefore measured by

the phtodiode providing the error signal for BS longitudinal control. Therefore most of the noise floor of the BS error signal is induced by the angular control noise.

4.5 The C5 noise budget

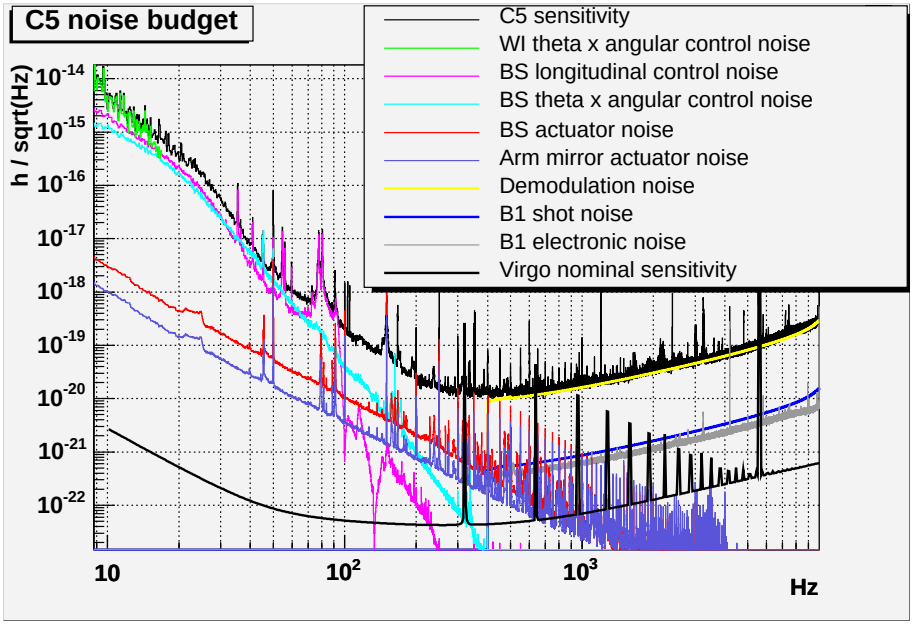

Figure 14: *Noise budget of the C5 run. The contribution of the angular control noise of the west input (WI) mirror is estimated from the coherence function between the corresponding correction signal and B1_ACp. The contributions of the beam splitter (BS) control noises are computed with the analytical models.*

The analysis of the sensitivity of the C5 run in the recycled configuration has provided the noise budget shown in Figure 14. In the low frequency region (between 10 and 100 Hz) the sensitivity is reasonably well explained by control noises, which are introduced by the beam splitter longitudinal control loop and by the angular local controls in θ_x of both beam splitter and west input mirrors. For what concerns the high frequencies, the analysis has shown that the C5 sensitivity is limited by demodulation noise which couples to the dark fringe signal through misalignments of the interferometer. This noise is about 20 times higher than the shot noise of the dark fringe signal. The sensitivity is not fully understood between 100 and 400 Hz: According to the estimation of the actuator noise obtained from a measurement done when no correction signal was sent to the DAC, actuator noise should not limit the sensitivity. Nevertheless this estimation migth be underestimated since an additional non linear noise has been discovered by analysing the sensitivities obtained during the commissioning runs performed since then.

5 Analysis of the C6 run sensitivity

The sensitivity obtained during the C6 run is analyzed in this section. The noise sources which are likely to have a significant impact in the sensitivity at high frequency such

as the dark fringe readout noises, the demodulation noise and the laser frequency noise are presented in 5.1, 5.2 and 5.3 respectively. The intermediate frequencies are limited by environmental noise as shown in 5.4. The contributions at low frequency of actuator noise and noise introduced by the control loops are discussed in 5.5 and 5.6 respectively.

5.1 Dark fringe readout noises

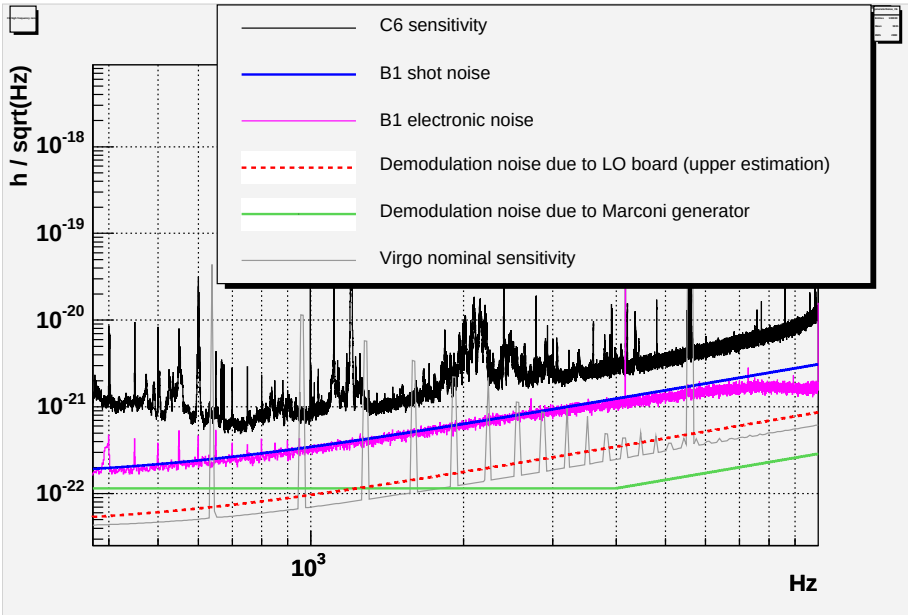

Figure 15: *Contribution of B1 readout noises in the C6 sensitivity.*

The B1 electronic noise has been measured by using the same method as that explained in 4.1. The B1 shot noise is evaluated from the DC power which reaches the photodiode during the C6 run ($P_{DC} \approx 1.4\,mW$). The contributions in sensitivity of the B1 electronic noise and the B1 shot noise are shown in Figure 15. Both contributions are about a factor 2.5 lower than the sensitivity curve above 1 kHz so that they can explain 40 % of the noise limiting the sensitivity in this frequency region. Another source of noise has therefore to be found in order to fully understand the high frequency part of the C6 sensitivity.

5.2 Demodulation noise

As shown in 4.2, the high frequency part of the C5 sensitivity was limited by the demodulation noise induced by the phase noise generated by the local oscillator (LO) boards. After the C5 run, as anticipated in section 4.2, the contribution of this noise has been reduced with the following upgrades:

- The electronic scheme of the LO board has been simplified to reduce its phase noise. A measurement performed in the same conditions as that of Figure 9 shows that the residual phase noise $\delta\phi_{dem}$ is smaller than 0.1 $\mu rad/\sqrt{Hz}$ (i.e. three times lower than for the C5 run). This upper limit is given by the intrinsic noise of the system used for the measurement.

- The alignment conditions have been improved thanks to the linear alignment which was partially implemented during the C6 run (as explained in 2). This resulted in the reduction of the $B1\_ACp$ signal by about a factor 35. As the coupling of the phase noise into the dark fringe signal is proportional to $B1\_ACq$ signal, the contribution in sensitivity of the demodulation noise (induced by both generator or LO board) is reduced by the same factor.

The impact in the C6 sensitivity of the demodulation noise induced by the generator has been computed by using relations (10) and (13). The result is compared to the C6 sensitivity in Figure 15. The upper limit for the contribution of the LO board phase noise is also shown. The contribution of the two kinds of demodulation noise remains lower than the C6 sensitivity by almost one order of magnitude so that they are not the dominant sources of noise. However they could prevent to reach the Virgo nominal sensitivity, especially in the range of frequencies between 100 Hz and 1 kHz where the impact of the Marconi generator phase noise exceeds the Virgo design by about a factor 2. This problem has been cured at the end of 2005 by replacing the Marconi generator by a LNFS-100 generator which is about ten times less noisy in this frequency range.

5.3 Laser frequency noise

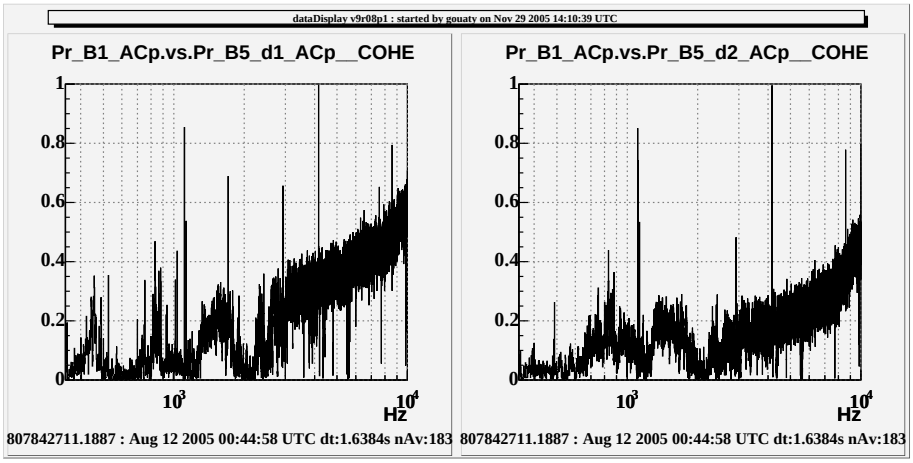

Figure 16: *Coherence function obtained during the C6 run between the dark fringe signal and respectively: the ACp signal of the $B5\_d1$ photodiode which is used as error signal of the laser frequency stabilisation loop (left plot), the ACp signal of the $B5\_d2$ photodiode which is out of loop (right plot).*

5.3.1 Identification and projection of the laser frequency noise

During the C6 run the dark fringe signal is coherent with the error signal of the frequency stabilization ($B5\_ACp$) above 1 kHz, indicating that frequency noise might limit the sensitivity. The beam B5 was shared equally on two photodiodes ($d1$ and $d2$) but the error signal is only extracted from $B5\_d1$. As is shown on Figure 16 the coherence with the dark fringe signal is not the same for these two photodiodes. This can be interpretated

by the fact that these photodiodes see different noises, as it is the case if these signals are dominated by their own readout noise. In this case the frequency stabilization corrects for $d1$ photodiode readout noise and therefore converts it into frequency noise. Due to the high unity gain (around 10 kHz) of this loop, this noise is therefore partially cancelled on $d1$. On the contrary the $d2$ photodiode which is out of loop gives a measurement of the laser frequency noise entering the interferometer through this loop. Consequently an estimation of the contribution in sensitivity of the laser frequency noise can be extracted from the coherence function measured between the dark fringe signal and the $B5\_d2\_ACp$ signal, according to the relation:

$$h \;=\; B1\_ACp \left(|| < B1\_ACp, B5\_d2\_ACp > || \right)^{\frac{1}{2}} \; k_{corrective} \; C_{W \rightarrow h} \qquad (26)$$

where $< B1\_ACp, B5\_d2\_ACp >$ is the complex coherence function between $B1\_ACp$ and $B5\_d2\_ACp$, $C_{W \rightarrow h}$ is the calibration transfer function, and $k_{corrective}$ is a corrective factor which is needed to compensate the underestimation of the coherence function due to the readout noises of the $B5\_d2$ photodiode. The incoherent sum of the electronic noise and the shot noise of the $B5\_d2$ photodiode is around a factor 0.75 lower than the signal measured on $B5\_d2\_ACp$ leading to a corrective factor $k_{corrective} \approx 1.5$.
The contribution in sensitivity of the laser frequency noise obtained from relation (26) is shown in Figure 17. It explains about 50 % of the noise limiting the high frequency part of the C6 sensitivity.

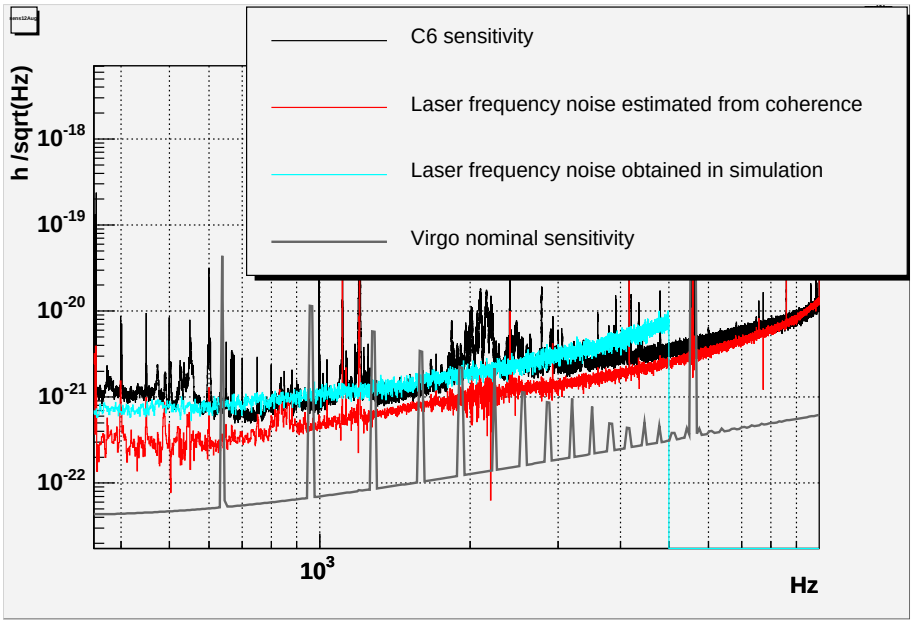

Figure 17: *Contribution of the laser frequency noise in the C6 sensitivity.*

5.3.2 Simulation of the laser frequency noise

As mentioned above, the laser frequency noise is suspected to originate from the readout noise of the $B5\_d1$ photodiode which propagates through the laser frequency stabilization

loop. This effect has already been observed in recombined configuration during the C4 run, as it is explained in [1].
During the C6 run the $B5\_d1$ photodiode was not calibrated so that it is not possible to project the impact of its readout noise on the sensitivity curve. Therefore a simulation study has been performed with SIESTA in order to check if the $B5\_d1$ photodiode readout noise is able to explain the laser frequency noise measured during the C6 run. The longitudinal control loops are implemented in the simulation according to the locking scheme shown in Figure 1. The electronic and shot noise are also included in the simulation. The propagation of the laser frequency noise into the dark fringe signal depends on the CMRF. The CMRF has been tuned in simulation so that it is equal to about 2×10^{-3} above a few hundred Hertz. This value is consistent with the measurement made in the recombined configuration (see section 4.2 of [1]).
The laser frequency noise obtained in simulation, induced by the electronic and shot noise of the B5 photodiode, is shown in Figure 17. Since the CMRF has not been measured for the recycled interferometer and the laser frequency stabilization loop is not perflectly tuned in simulation, this result only provides an order of magnitude of the contribution in sensitivity of the $B5\_d1$ readout noise. Nevertheless the prediction obtained with this simulation gives the same order of magnitude and behaviour as expected from the coherence function. This confirms the hypothesis according to which the laser frequency noise observed during the C6 run is induced by the $B5\_d1$ photodiode readout noise.

As shown in Figure 34 the sum of all high frequency noises discussed in the previous sections (B1 readout noise and laser frequency noise) explains well the noise floor of C6 sensitivity from 600 Hz to 10 kHz. Nevertheless several noise structures visible in the sensitivity curve below 3 kHz are not explained by these noises and are investigated in the next section.

5.4 Environmental noise

Most of the noise structures visible in the sensitivity curve between 100 Hz and 3 kHz have been identified as environmental noise originated from different places:

- Environmental noise in the laser laboratory is found to be responsible for the power noise visible in the dark fringe signal as shown in 5.4.1.
- Environmental noise due to the detection turbo pump produces vibrations of the detection external bench as it is shown in 5.4.2.
- Environmental noise in the north end building enters the interferometer through spurious reflected beams as it is shown in 5.4.3.

5.4.1 Power noise at the exit of the input mode cleaner

During the C6 run some coherence has been observed in the 200 Hz - 1kHz frequency range between the dark fringe signal and the signal which monitors the DC power transmitted by the input mode cleaner cavity (see Figure 18). This indicates that the sensitivity might be limited by the power fluctuations of the beam entering the interferometer.

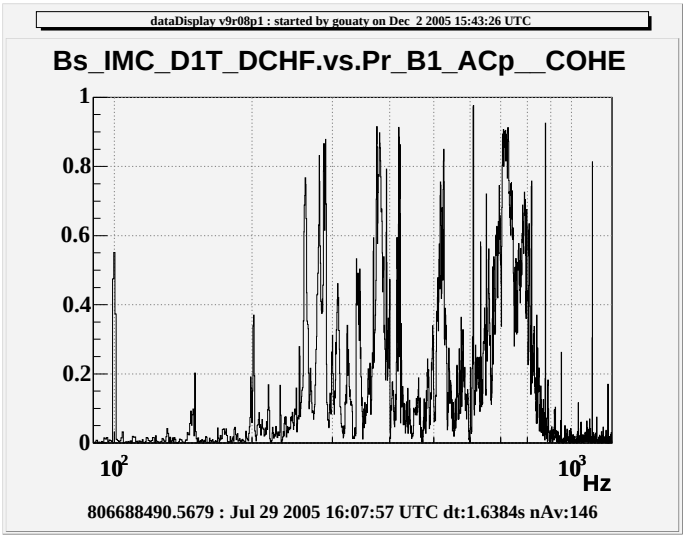

Figure 18: *Coherence function computed between the dark fringe signal and the DC power transmitted by the input mode cleaner cavity at the beginning of the C6 run (July* 29^{th}*, 2005).*

An hypothesis which can explain power fluctuations at the exit of the input mode cleaner cavity consists in assuming that the incident beam reaching the entrance of the input mode cleaner cavity is subject to slight fluctuations of its position and orientation. This phenomenon is called beam jitter. The beam jitter can be induced by environmental noise in the laser laboratory (such as acoustic or seismic noise). This beam jitter modifies the matching between the incident beam and the beam resonating inside the mode cleaner cavity, so that it produces power fluctuations of the transmitted beam.
An analytical model which propagates the power fluctuations to the dark fringe signal has to be found in order to check if this noise (referred to as power noise in the following) actually limits the C6 sensitivity.

Analytical model for the propagation of power noise

The interferometer is locked on the dark fringe with an accuracy which depends on the loop gain and the alignment conditions of the interferometer. The power fluctuations $\delta\tilde{P}$ couples to the dark fringe proportionally to these residual fluctuations from the real dark fringe. It produces a signal which is equivalent to a differential motion of the end mirrors given by:

$$\delta\tilde{l} \;=\; \frac{\Delta\tilde{l}_0 \otimes \delta\tilde{P}}{P_{DC,0}} \tag{27}$$

where:

- $\Delta\tilde{l}_0$ (which gives the locking accuracy) refers to the difference of length between the two cavities (including a possible static deviation from the dark fringe condition)
- $P_{DC,0}$ is the mean value of the power.

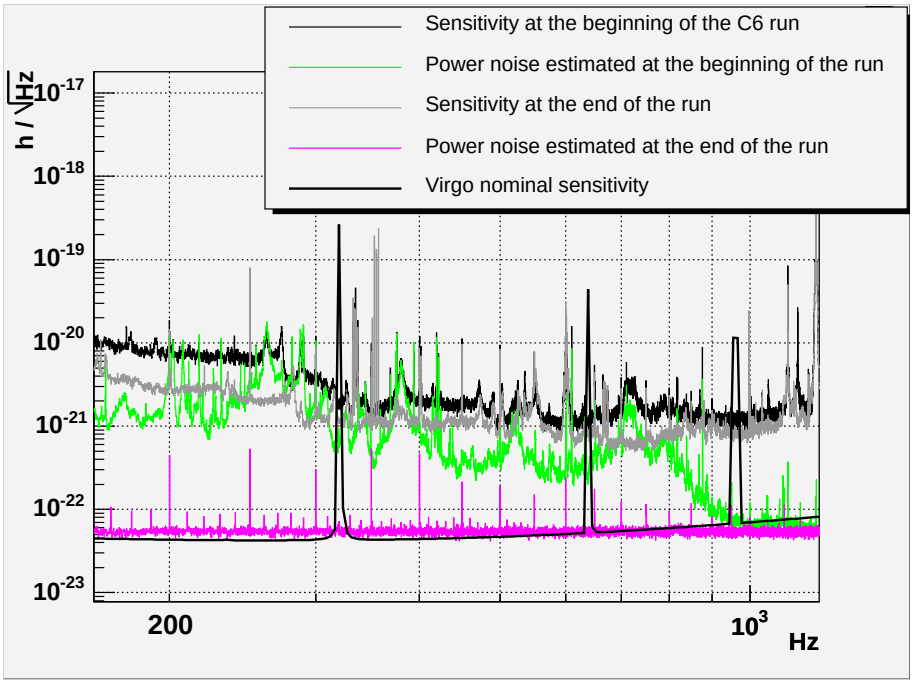

Figure 19: *Contribution of power noise to the sensitivity. The situation at the beginning of the C6 run (29^{th} of July) is compared to the situation obtained at the end of the run (12^{th} of August) after reduction of power noise.*

- The symbol $\otimes$ represents the convolution integral.

Since the locking accuracy is dominated by low frequency (limited to a few Hertz) variations, the previous equation can be approximated by:

$$\delta\tilde{l} \;=\; \frac{\delta\tilde{P}}{P_{DC,0}} \int_0^{f_0} \Delta\tilde{l}_0 df \tag{28}$$

In equation (28) the frequency f_0 represents the upper limit of the considered frequency range ($f_0 < 20\ Hz$) for $\Delta\tilde{l}_0$. The locking accuracy $\Delta l_{rms} = \int_0^{f_0} \Delta\tilde{l}_0 df$ can be estimated with the RMS of the dark fringe spectrum (as this signal measures the difference of length between the two arms), converted into meters with the calibration transfer function. It has been estimated using either B1 or B1p:

- Using $B1\_ACp$ it gives: $\Delta l_{rms} \approx 0.2 \times 10^{-12}\ m$. However it has to be mentioned that this estimation is likely to be underestimated in presence of mirror angular motions. Indeed low frequency angular motions of the mirrors can generate a beam jitter which couples to $B1\_ACp$ through the output mode cleaner cavity, and then can be reintroduced as low frequency length noise by the differential mode control loop. This length noise is not measured by $B1\_ACp$ since it tends to cancel the effect of the angular motions.

- A conservative estimation can be obtained by using the $B1p\_ACp$ signal which is also sensitive to the difference of length between the two arms but is not filtered by the output mode cleaner. This methods provides: $\Delta l_{rms} \approx 5 \times 10^{-12}\ m$. This

estimation is likely to be overestimated since this signal is polluted by high order modes.

Finally one can expect that the real locking accuracy lies between the two previous estimations: $0.2 \times 10^{-12}\ m \leq \Delta l_{rms} \leq 5 \times 10^{-12}\ m$.
The value of Δl_{rms} has been taken equal to $2 \times 10^{-12}\ m$ in order to adjust the estimation of power noise given by relation (28) to the sensitivity curve obtained at the beginning of the C6 run for the frequencies where the coherence shown in Figure 18 is near to one. The value choosen for Δl_{rms} belongs to the expected range and is therefore realistic. As it is shown in Figure 19, power noise explains several noise structures visible in the sensitivity curve obtained at the beginning of the run between 200 Hz and 1 kHz.

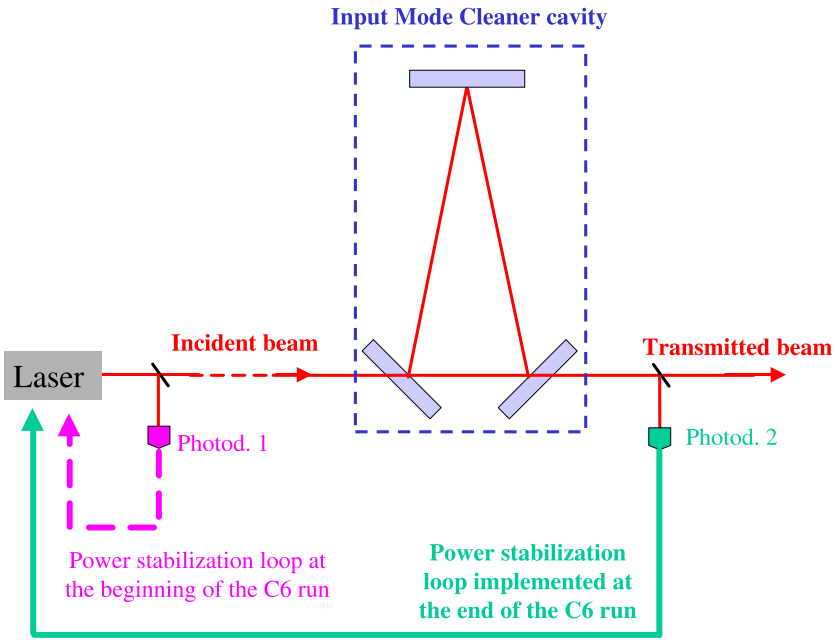

Figure 20: *Simplified scheme of the power stabilization loop used before and after the upgrade of the C6 run.*

Reduction of power noise during the C6 run

As the power noise was identified as a noise source limiting the sensitivity curve at the beginning of the C6 run, the two following actions were performed by the commissioning team during the run in order to reduce the impact of power noise:

- The beam reaching the input bench was realigned with respect to the input mode cleaner (IMC), which, by improving the matching between the incident beam and the beam resonating inside the IMC cavity, reduces the sensitivity of the IMC to beam jitter.

- The power stabilization loop has been upgraded. The feedback used at the beginning of the C6 run as well as the new feedback implemented at the end of the run

are shown in Figure 20. The only difference between the two strategies concerns the error signal. At the beginning of the C6 run, the error signal of the power stabilization loop was built from a signal provided by a photodiode located on the laser bench (denoted as "photod. 1" in Figure 20), so that the feedback was not able to cancel the power fluctuations at the exit of the IMC cavity. Accordingly the previous error signal was replaced by the signal delivered by "photod. 2", located after the IMC.

These technical upgrades have allowed the reduction of power noise, so that, at the end of the run, no coherence is visible between the dark fringe signal and the signal measuring the power transmitted by the IMC cavity. This permits the improvement of the sensitivity shown in Figure 19: the noise structures which were related to power noise at the beginning of the run are suppressed. The level of the remaining power noise, estimated by using the same model as that given by relation (28) with $\Delta l_{rms} = 2 \times 10^{-12} m$ is shown in Figure 19: it is comparable to the Virgo nominal sensitivity. Nevertheless it can be expected that the locking accuracy improves with the implementation of the full linear alignment so that this noise remains lower than the Virgo design sensitivity.

5.4.2 Vibrations of the detection external bench

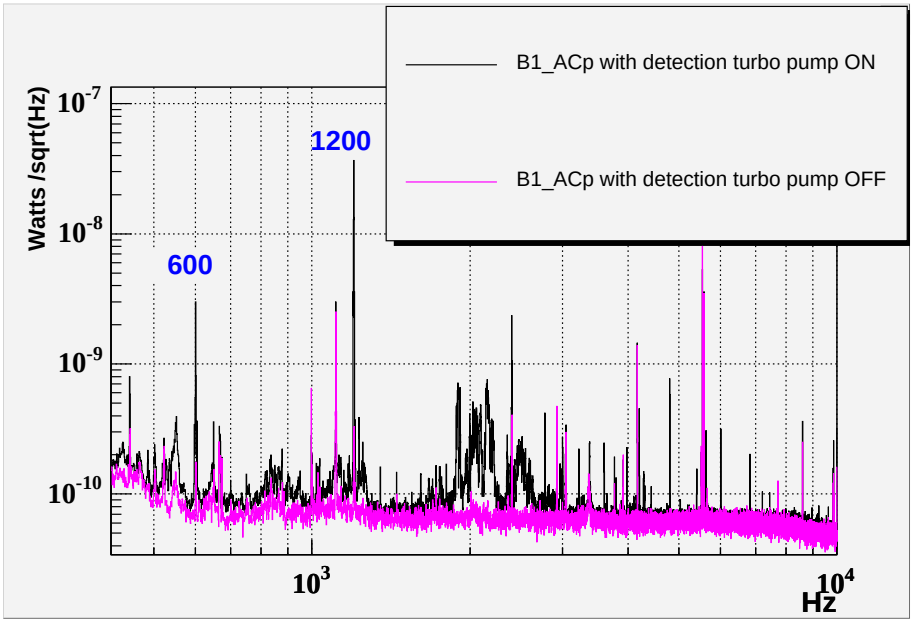

Figure 21: *Comparison between the high frequency spectrum of the dark fringe signal (B1_ACp) obtained when the detection turbo pump is running, and when the detection turbo pump is switched off. Both curves are computed with the data of the* 25^{th} *of August.*

A test performed on vacuum turbo pumps after the C6 run allowed the understanding of the origin of the noise structure visible in the C6 sensitivity between 1800 and 3000 Hz (which is referred to as the "2 kHz structure" in the following) as well as the big resonances visible at 600 and 1200 Hz.
This test consisted into switching off progressively all the turbo pumps in order to check if

some noise in the sensitivity could be correlated to the pump operation. It was found that the 2 kHz structure visible in the sensitivity curve during the C6 run fully disappears when the turbo pump of the detection tower is stopped, as it is shown in Figure 21. Moreover a similar noise structure can be reproduced by injecting acoustic noise in the detection laboratory, which tends to indicate that the 2 kHz structure must not be related to the pump itself but to some mechanical resonances of the detection external bench which are excited by the pump. This shows that it will be needed to isolate the detection bench from mechanical vibrations in order to reach the Virgo nominal sensitivity.
The big resonances at 600 Hz and 1200 Hz visible in the C6 sensitivity are also related to the turbo pumps operation, as they correspond to the rotation frequency of the pumps and to its first harmonic, respectively. As it is shown in Figure 21 the 600 Hz resonance is reduced by a factor 20 and the 1200 Hz resonance by a factor 100 when the detection turbo pump is not running. One can conclude that the main contribution to these resonances is due to the detection turbo pump.

5.4.3 Impact of spurious reflected beams

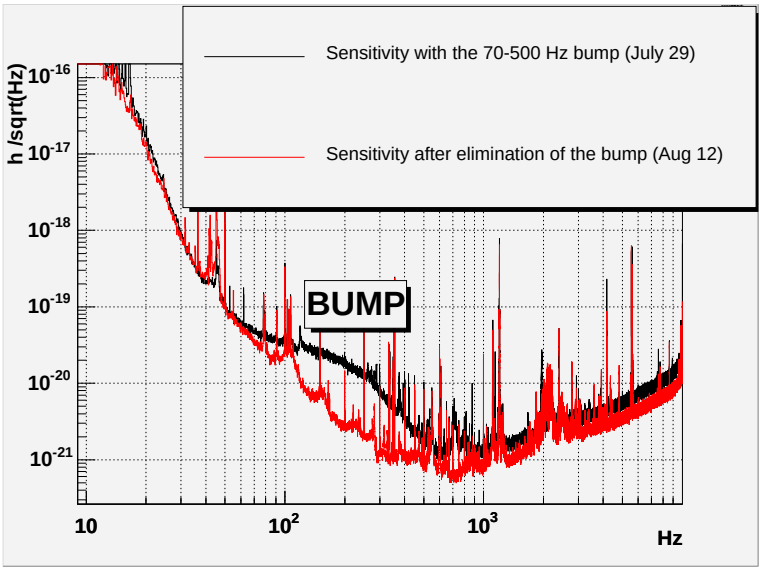

Figure 22: *Comparison between the sensitivity obtained at the beginning of the C6 run (July* 29^{th}*) and the sensitivity obtained at the end of the C6 run (August* 12^{th}*). The most impressive difference between the two curves is the 70-500 Hz bump which is visible in the sensitivity of July* 29^{th}*.*

At the beginning of the C6 run a bump was visible in the sensitivity curve between 70 and 500 Hz, as shown in Figure 22. The analysis presented in the following showed that this bump was related to spurious reflected beams on the external bench of the north end building.
One characteristic of the 70-500 Hz bump is its non stationarity. This is shown in Figure 23 where the RMS of the 323 Hz component of $B1\_ACp$ spectrum (which gives the typical behaviour of the bump) is plotted as a function of time. It can be noticed that the amplitude of the bump varies with a periodicity of about 40 minutes. These variations

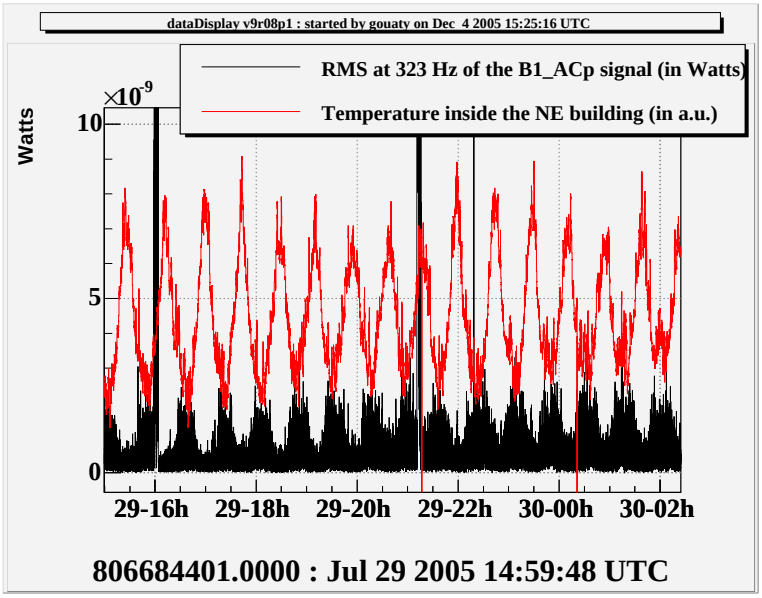

Figure 23: *Comparison between the RMS of the 323 Hz component of the B1_ACp spectrum and the temperature measured by a sensor located in the north end building. The data correspond to the beginning of the C6 run. The temperature oscillates between 22.5 and 24.5°c with a periodicity of about 40 minutes. The variations in time of the RMS at 323 Hz of B1_ACp are correlated with the temperature fluctuations.*

are correlated to the temperature fluctuations measured by a sensor located in the north end building. This indicates that the bump is coupled with environmental noise inside this building. This hypothesis is confirmed by the observation of coherence between the dark fringe signal and the demodulated signals of the B7 photodiode in the frequency region of the bump. This photodiode, which receives the beam transmitted by the north end mirror, is located on the optical bench of the north end building.
The previous observations, performed at the beginning of the C6 run, have allowed the identification of the place where the noise responsible for the 70-500 Hz bump was generated. An examination of the optical bench of the north end building spotted out some spurious reflected beams. These stray beams have been damped during the run. The non stationary noise disappeared after this intervention. The resulting improvement in sensitivity can be seen in Figure 22. One can conclude that the noise associated to the bump at the beginning of the C6 run was coupled to the dark fringe signal through the spurious reflected beams generated on the optical bench of the north end building.

5.5 Actuator noise

5.5.1 Mirror actuator noise with the standard method

A first estimation of the contribution to the C6 sensitivity of the mirror actuator noise is obtained by using the same method as that presented in 4.2.1 for the C5 run. This method, referred to as the "standard method" in the following, relies on the measurement of the coil current performed in January 2005 on eight coils of the arm towers when no correction signal is sent to the DAC, which provides: $\delta u = 440\ nV/\sqrt{Hz}$. It should

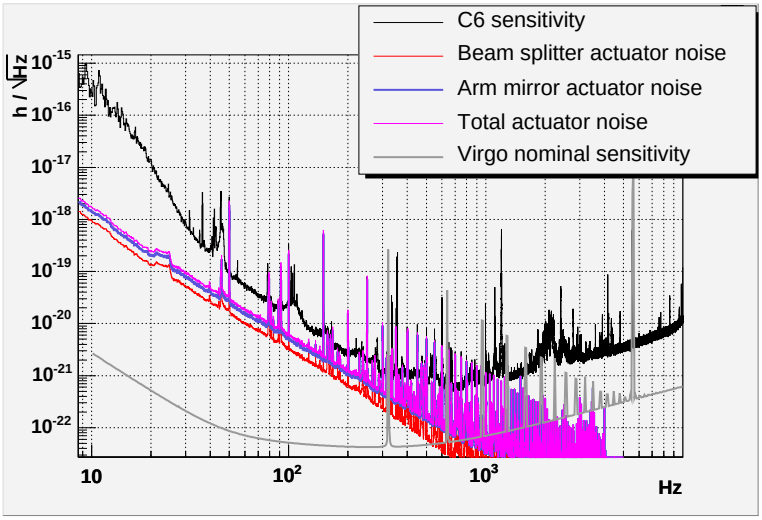

Figure 24: *Standard estimation of the actuator noise during the C6 run.*

be mentionned that another measurement performed on four other coils rather gave a value almost 20 % lower. The most conservative value has been kept for the following estimations.
The relations (15) and (16), which were used to compute the contribution to the C5 sensitivity of the arm mirror actuator noise and of the beam splitter actuator noise respectively, have to be slightly updated in order to take into account the following modifications:

- During the C6 run sixteen coils are plugged in the arm towers instead of eight (as it was during the C5 run), so that the contribution of the arm mirror actuator noise is increased by a factor $\sqrt{2}$ with respect to the C5 run, which gives:

$$h = \left|\left|\frac{1}{L}\sqrt{16}\ k_a.K_{DC}.E.M.\delta\tilde{u}\right|\right| \tag{29}$$

  The parameters used in relation (29) are the same as those of relation (15).

- The electronics of the beam splitter actuators has been upgraded by adding a serial resistor R_{serie} of 32 Ω with each coil, so that the controbution in sensitivity of the beam splitter actuator noise is now given by:

$$h = \left|\left|\frac{1}{L}\sqrt{4}\sqrt{2}\frac{\pi}{2F}\ k_a.K_{DC}.E.M.\delta\tilde{u}\right|\right| \tag{30}$$

  with $k_a = \frac{R_{coil}}{R_{coil}+R_{serie}} \approx \frac{1}{3.9}$. The value of the conversion factor K_{DC} has been measured after this modification with the same method as for C5 (see section 4.3) and gives $K_{DC} = 27 \pm 6\ \mu m/V$. This upgrade allows the reduction of the beam splitter actuator noise by about a factor 4.

The results obtained with equations (29) and (30) are shown in Figure 24. The total actuator noise, which is obtained by summing quadratically the contributions of beam splitter actuator noise and arm mirror actuator noise, remains between a factor 2 and a factor 3 lower than the sensitivity curve. Nevertheless it was shown that this method underestimates the actuator noise, as explained in the following.

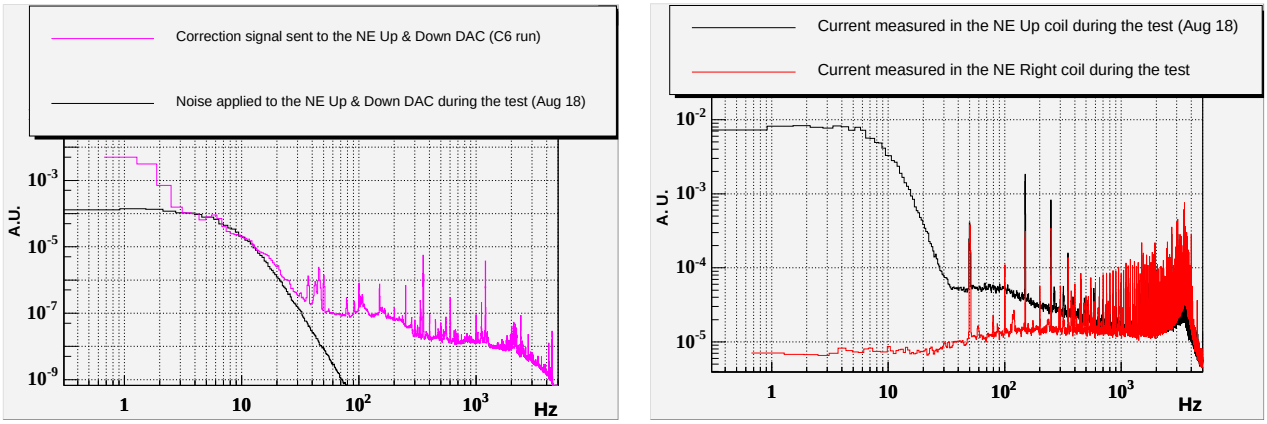

Figure 25: *Evidence of non linear actuator noise (test performed on August* 18^{th}*). In the left plot, the spectrum of the noise applied to the DAC input of the north end (NE) "Up" and "Down" coils is compared to the correction signal which was sent to the same DAC during the C6 run. In the right plot the spectra of the currents measured respectively on the north end "Up" coil and the north end "Right" coil during the test are compared.*

5.5.2 Mirror actuator noise including non linear effects

Several experiments performed after the C6 run have pointed out that a non linear noise appears in the coil current when a low frequency signal is sent to the DAC. For example when a line at 250 mHz is applied to the DAC, the full spectrum of the current measured in the corresponding coil is spoiled by harmonics of the 250 mHz line, which indicates a non linear effect. Moreover the amplitude of the harmonics increases if the amplitude of the line sent to the DAC increases. This means that the actuator noise measured when no correction signal is sent to the DAC must be underestimated.
A test has been performed on August 18^{th} in order to estimate the level of the non linear noise for the coils used by the locking control loops to apply forces on the mirrors. Two coils (denoted as the "Up" and "Down" coils) are concerned for each end arm mirror. The test consisted in measuring the coil current when a low frequency noise simulating the effect of the correction signal is applied to the DAC input. The test was performed on the "Up" and "Down" coils.
In the left plot of Figure 25 the noise sent to the DAC during the test is compared to the spectrum of the correction signal sent to the north end mirror during the C6 run. The spectrum of the current measured in the north end "Up" coil during the test is shown in the right plot of Figure 25. The low frequency part of this spectrum corresponds to the DAC input signal, whereas the frequencies above 40 Hz are dominated by actuator noise. The spectrum of this coil current is compared to the spectrum of the "Right" coil current whose DAC does not receive any signal and gives a measurement of the standard actuator noise. This shows the presence of a non-linear noise which depends on the input signal sent to the DAC.
To summarize, when a signal similar to the locking signal is applied to the DAC the actuator noise observed varies from about 2400 $nV/\sqrt{Hz}$ at 50 Hz (i.e. about 5.5 times more than the standard actuator noise) to about 440 $nV/\sqrt{Hz}$ at 500 Hz (which corresponds to the level of the standard actuator noise).

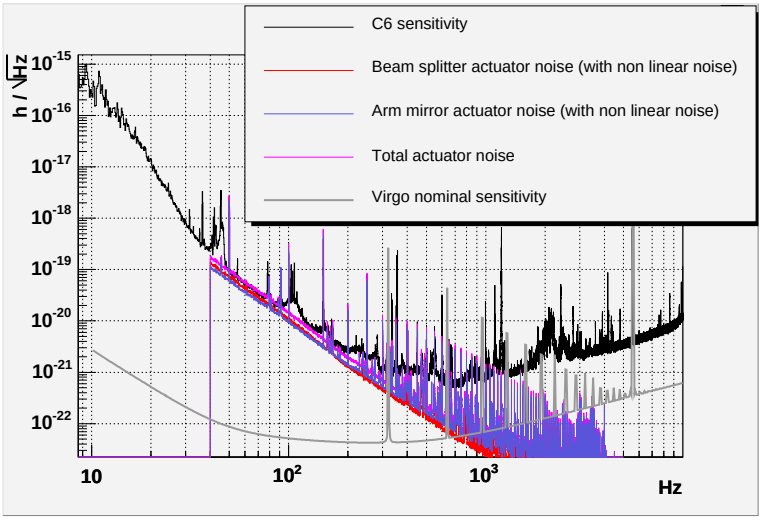

Figure 26: *Updated estimation of the actuator noise during the C6 run. The non linear noise of the "Up" and "Down" coils for both end mirrors is extracted from the measurement performed on August* 18^{th}*. The non linear noise associated to the beam splitter coils has not been directly measured, but is extrapolated from the measurement done for the end arm mirrors.*

The contribution in sensitivity of the arm mirror actuator noise is obtained by adding quadratically the contribution of the four driven coils and the contribution of the twelve other coils (which are plugged but not driven):

$$h = \left(\left\| \frac{1}{L}\sqrt{12}\ k_a.K_{DC}.E.M.\delta\tilde{u} \right\|^2 + \left\| \frac{1}{L}\sqrt{4}\ k_a.K_{DC}.E.M.\delta\tilde{u}_{nl} \right\|^2 \right)^{\frac{1}{2}} \qquad (31)$$

where δu_{nl} refers to the non linear noise. For the four beam splitter coils (which are all driven), the non linear noise is supposed to be the same for each coil as that measured in the end arm towers, since the spectrum of the correction signal sent to the beam splitter DAC during the C6 run is similar to the spectrum of the end mirror correction signals for frequencies between 3 Hz and 30 Hz. Consequently the contribution in sensitivity of the beam splitter actuator noise is obtained by replacing δu by δu_{nl} in relation (30).
The results provided by these models are shown in Figure 26. The estimated contributions of the beam splitter actuator noise and of the arm mirror actuator noise have similar amplitudes. Their quadratic sum fits quite well to the sensitivity floor between 50 and 200 Hz, so that it can be concluded that the actuator noise is the main source of noise limiting the sensitivity in this region of frequencies.
Several actions have been planned in order to reduce the contribution in sensitivity of mirror actuator noise:

- The non linear noise induced by the correction signals sent to the DAC can in principle be reduced with a better tuning of the actuator electronics.
- The standard actuator noise can be lowered by increasing the value of the serial resistor R_{serie}. However, as it has been explained in [1], this method is limited by the dynamic range of the locking correction signals. Indeed, during the C6 run, the

value of R_{serie} could not be increased any more on the end arm mirrors because the corrections sent to the DAC were close to the saturation voltage. This problem can be solved with the implementation of the hierarchical control. It consists in allocating the low frequency part of the correction signal to the marionette, thus the dynamic range of the corrections applied to the mirrors can be reduced. This then allows the increase of the serial resistor R_{serie}.

5.6 Noise introduced by the control loops

Two different longitudinal control loops have been identified as sources of noise during the C6 run: the beam splitter longitudinal control loop which introduces noise in the dark fringe signal below 50 Hz as shown in 5.6.1, and the power recycling mirror longitudinal control loop which seems to have an impact on the sensitivity curve between 100 and 500 Hz as shown in 5.6.2. The impact of angular control noises below 30 Hz is discussed in 5.6.3.

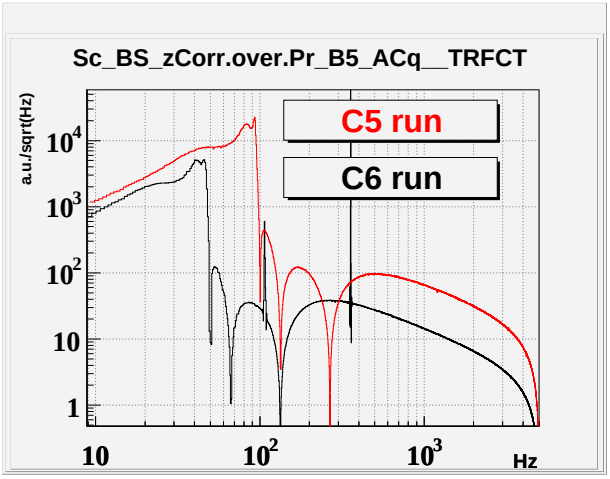

Figure 27: *Comparison between the transfer function modulus of the filter implemented in the beam splitter (BS) longitudinal control loop during the C5 run and during the C6 run. These curves have been obtained by measuring the transfer function between the error signal B5_ACq and the correction signal BSzCorr sent to the beam splitter mirror.*

5.6.1 Beam splitter longitudinal control noise

As it has been shown in 4.4.3, the sensitivity obtained during the C5 run was partially limited by the beam splitter longitudinal control noise in the low frequency region (below 100 Hz). Between the C5 run and the C6 run, two kinds of upgrades have been performed in order to reduce the contribution of this noise in the sensitivity: the improvement of the numerical filter of the beam splitter control loop, and the implementation of an additional feedback referred to as the α technique. These improvements and their consequences are described here.

The numerical filter used for the beam splitter longitudinal control loop has been improved. This filter receives the error signal $B5\_ACq$ as input and provides the correction

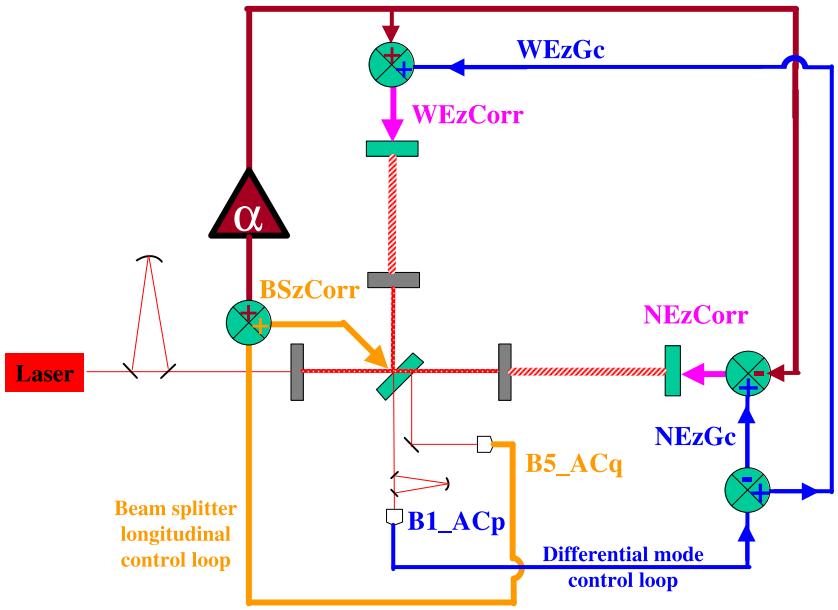

Figure 28: *Scheme of the beam splitter longitudinal control loop and the end arm mirrors longitudinal control loop including the "α technique". The other locking control loops have been omitted for legibility reasons.*

signal $BSzCorr$ as output. The transfer function modulus of the filters implemented during the C5 and C6 runs are compared in Figure 27. A roll-off filter is used which gives the sudden decrease of the transfer funcion modulus at the so called roll-off frequency. The improvement has consisted in lowering the frequency of the roll-off from 100 Hz to 50 Hz which allows the reduction of the noise introduced by this control loop by at least a factor 100 between 50 and 100 Hz.

An additional control loop, shown in Figure 28, has been implemented in the locking scheme, in order to reduce the impact of the beam splitter control noise to the sensitivity. This strategy, which is called the "α technique", aims at cancelling the effect on the dark fringe signal of the noise introduced by the beam splitter longitudinal control loop by sending appropriate correction signals to the end arm mirrors. These signals, denoted as NEzCorr and WEzCorr, are given by the following relations:

$$\begin{aligned} NEzCorr &= NEzGc - \alpha BSzCorr \\ WEzCorr &= WEzGc + \alpha BSzCorr \end{aligned} \tag{32}$$

where NEzGc and WEzGc are the corrections built from the error signal $B1\_ACp$ of the differential mode control loop, whereas the product $\alpha BSzCorr$ is the additional correction used to compensate the effect of the beam splitter longitudinal control noise. The α coefficient represents the coupling factor between the beam splitter longitudinal control noise and the equivalent difference of length between the two Fabry Perot cavities. It has been tuned empirically by trying to minimize the noise seen in the dark fringe signal.

The two upgrades previously mentioned were implemented before the C6 run. As can be

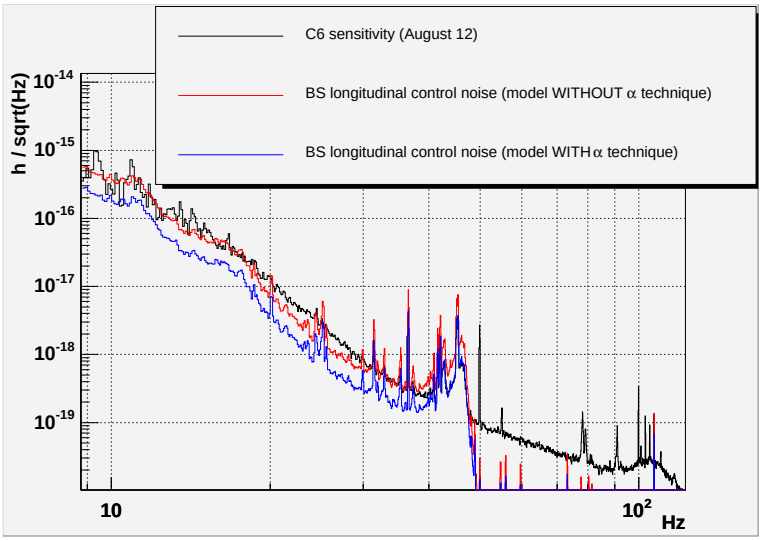

Figure 29: *Contribution of the beam splitter longitudinal control noise in the C6 sensitivity (August* 12^{th}*). The model taking into account the* α *technique is obtained with a* α *coefficient mistuned by* 45 %*.*

observed from Figure 2, between C5 and C6 the sensitivity has improved by more than an order of magnitude in the frequency range where the beam splitter longitudinal noise was dominant (i.e. up to 100 Hz). Nevertheless some coherence is still observed between the dark fringe signal and the beam splitter longitudinal correction signal, especially in the frequency region between 30 and 50 Hz where some structures (at 31.5 Hz, 35.5 Hz and 42 Hz) correspond to the input bench mechanical resonances already mentionned in 4.4.2. Some additional structures (at 36.5 Hz and 45 Hz), which were not observed during the C5 run, are now visible in the spectrum of the beam splitter longitudinal correction signal. These structures are also visible in the signals of the laser frequency stabilization loop as well as in the correction signals sent to the end mirror of the input mode cleaner, which indicates that they might also be related to the injection system.
The sensitivity curve obtained at the end of the run between 10 and 100 Hz is shown in Figure 29 where it is compared to two different estimations of the beam splitter longitudinal control noise.
The first of these estimations is obtained from the analytical model presented in 4.4.2:

$$\delta l_{noise} \;=\; \left|\left|\sqrt{2}\frac{\pi}{2F}2K_{DC}.E.M.BS\tilde{z}Corr\right|\right| \tag{33}$$

This model does not take into account the effect of the α technique. Therefore it only gives an upper estimation of the contribution in sensitivity of the beam splitter longitudinal control noise. This model is about a factor 2 higher than the sensitivity curve in the region between 40 and 50 Hz, which shows that the sensitivity is improved by the α technique. As the resonances are still visible in the sensitivity curve between 30 and 50 Hz, this means that the α coefficient is not perfectly tuned with respect to its optimal value α_0. The residual contribution in sensitivity of the beam splitter longitudinal control noise can

be written as:

$$\delta l \;=\; \Big|1 - \frac{\alpha}{\alpha_0}\Big|\delta l_{noise} \;=\; \epsilon \delta l_{noise} \tag{34}$$

The mistuning ϵ of the α coefficient can be estimated by adjusting the model given by relation (34) to the measured sensitivity for the frequencies associated to the input bench mechanical resonances. This method has provided the second estimation of beam splitter longitudinal control noise shown in Figure 29, with $\epsilon \approx 0.45$, which corresponds to a very large mistuning. Such a bad tuning seems to be due to the fact that the optimum value for α, which is empirically determined, can vary in time and α was only tuned at the beginning of the run.
According to the estimation which takes into account the effect of the α technique in Figure 29, the beam splitter longitudinal control noise still limits the sensitivity only in the region between 30 and 50 Hz, but is not able to explain the sensitivity obtained at lower frequencies, for which the noise estimation remains at least a factor 2 lower than the measured sensitivity.
The contribution of the beam splitter longitudinal control noise can be reduced by a better tuning of the α coefficient as is shown in 6.3.2.

5.6.2 Power recycling mirror longitudinal control noise

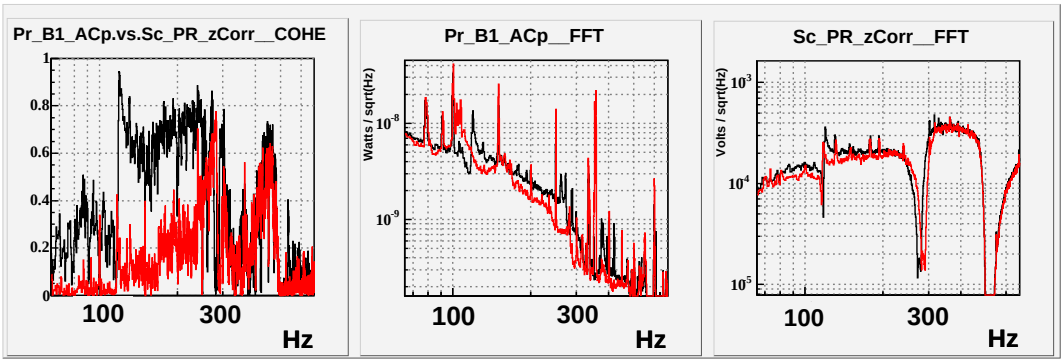

Figure 30: *Identification of the power recycling mirror longitudinal control noise: Comparison between the situation at the beginning of the run (July 29^{th}, black curves) and the situation at the end of the run (August 12^{th}, red curves). The left plot shows the coherence function between the dark fringe signal and the longitudinal correction signal sent to the power recycling mirror. The middle plot shows the spectrum of the dark fringe signal and the right plot shows the spectrum of the correction signal.*

At the beginning of the C6 run a high level of coherence (above 60 %) has been observed between the dark fringe signal and the longitudinal correction signal sent to the power recycling mirror in the region between 115 and 300 Hz as well as in the region between 400 and 500 Hz, as shown on the left plot of Figure 30. As no equivalent coherence can be found with other channels in this region of frequencies, this indicates that the power recycling longitudinal control loop might introduce a noise which propagates to the dark fringe signal.

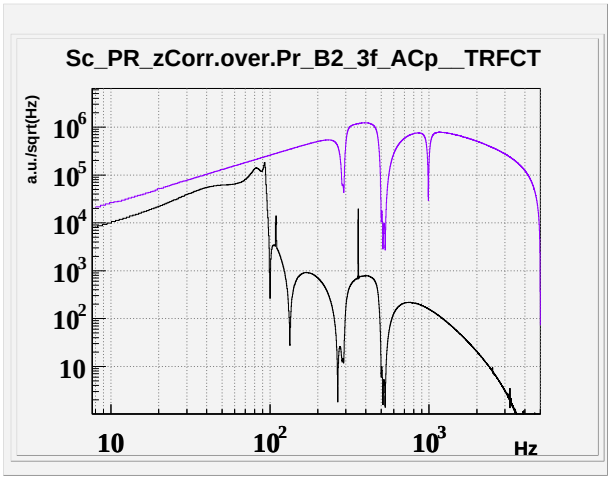

Figure 31: *Comparison between the transfer function modulus of the filter implemented in the power recycling longitudinal control loop during the C6 run (purple curve) and after the post C6 run upgrade (black curve). These curves have been obtained by measuring the transfer function between the error signal $B2\_3f\_ACp$ and the correction signal sent to the power recycling mirror.*

The level of coherence changes during the C6 run as shown in the left plot of Figure 30 where the coherence obtained at the beginning of the run (July 29^{th}) is compared to that at the end of the run (August 12^{th}) which is strongly reduced between 115 and 250 Hz. The spectrum of the dark fringe signal and the spectrum of the correction signal sent to the power recycling mirror are shown respectively in the middle plot and in the right plot of Figure 30. One can notice that in the region between 160 and 300 Hz the noise visible in the dark fringe signal is lowered by a factor ranging between 1.5 and 2 on August 12^{th}, whereas the spectrum of the power recycling correction signal remains the same. This observation shows that the coupling to the dark fringe signal is smaller during the second period. This phenomenon could be interpretated as the effect of an improvement of the alignment conditions at the end of the run, noticing that the longitudinal motion of the power recycling mirror is equivalent to a common mode length variation of the short Michelson arms. By analogy with the effect of a common mode length variation of the Fabry Perot cavities which has been examined in section 3, one can expect that the coupling between the power recycling longitudinal motion and the dark fringe signal depends on the difference of reflectivity between the two arms. This difference of reflectivity is likely to be generated by mirror misalignments as these increase the mismatching between the beam resonating inside the recycling cavity and those resonating in the Fabry Perot cavities.
After the C6 run, the numerical filter implemented in this control loop has been modified in order to prevent the noise from propagating through this loop. The upgraded filter is compared to the filter used during the C6 run in Figure 31. A roll-off at 100 Hz is implemented in the upgraded filter which allows the reduction of the noise which could enter the interferometer above 100 Hz by about three orders of magnitude. After this improvement the coherence between the dark fringe signal and the correction sent to the power recycling mirror fully disappeared. This confirms the fact that some noise was

really introduced in the dark fringe signal through this control loop during the C6 run.

5.6.3 Noise introduced by the angular control loops

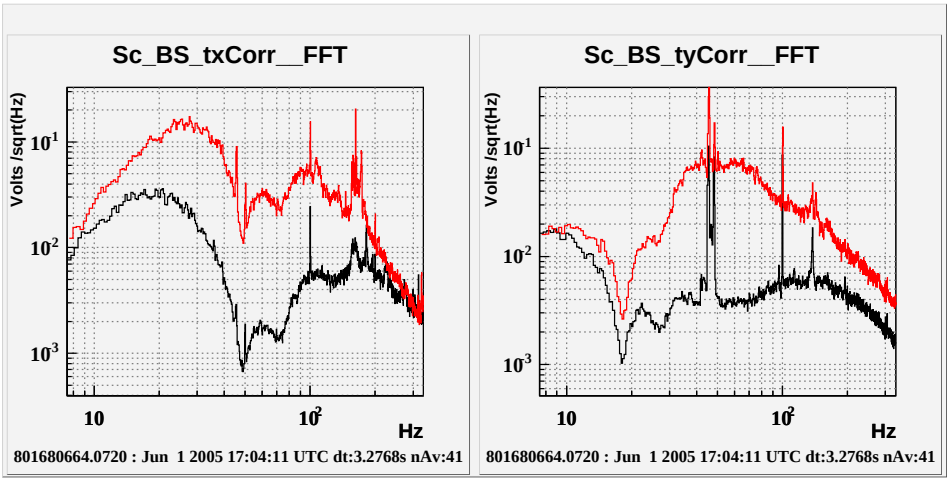

Figure 32: *Comparison between the spectrum of the beam splitter angular correction signals measured before (red) and after (black) the upgrade of the numerical filter.*

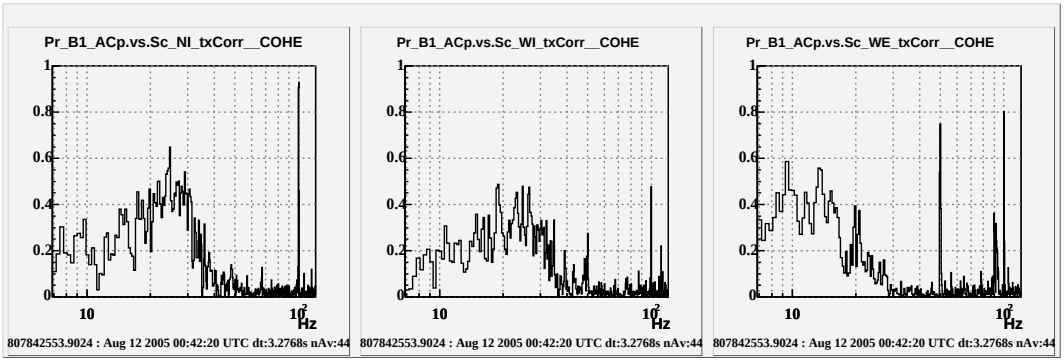

Figure 33: *Coherence functions obtained during the C6 run (August*12^{th}*) between the dark fringe signal and (from left to right): the* θ_x *angular correction signal sent to the north input mirror, the* θ_x *angular correction signal sent to the west input mirror, and the* θ_x *angular correction signal sent to the west end mirror. All these control loops are under local control for the frequency region of interest.*

The analysis of the C5 sensitivity presented in section 4 has shown that the low frequency part of the sensitivity was limited by noise introduced by the local control loops implemented in the beam splitter tower and in the west input tower to control the θ_x angular degree of freedom of the mirrors. Some technical improvements performed between the C5 run and the C6 run have allowed the reduction of these angular control noises as explained in the following.

For what concerns the beam splitter angular control noise, the main improvement has

been obtained by upgrading the numerical filter implemented in the control loop. The result of this upgrade is shown in Figure 32 where the spectrum of both θ_x (left plot) and θ_y (right plot) angular correction signals measured before and after the optimization of the filter are compared (θ_y refers to the angular motion around the vertical axis of the mirror). This upgrade allows the reduction of the noise introduced by the beam splitter angular control loops by about one order of magnitude between 20 and 100 Hz.
The north input and west input θ_x angular control noises have also been reduced by optimizing the numerical filter and the gain of the loops.

Thanks to the upgrades previously mentioned, the coherence between the dark fringe signal ($B1\_ACp$) and the beam splitter angular control noise disappears during the C6 run. However some coherence can still be found between $B1\_ACp$ and the θ_x angular correction signals sent to the north input, west input and west end mirrors for frequencies below 30 Hz, as shown in Figure 33. The maximum level of these coherences is around 40 %, but as these correction signals are not coherent between each other, their contributions in sensitivity can be added quadratically, so that the sensitivity can be reasonably well explained between 10 and 30 Hz with these three local control noises.
It has to be mentioned that some coherence has also been found between $B1\_ACp$ and the angular correction signals sent to the north end mirror, which is under linear alignment as explained in section 2. As these correction signals are also coherent with the θ_x correction signal sent to the west end mirror, one can suspect that the north end angular control loops do not introduce noise but that the noise induced by the west end mirror θ_x control loop is seen by the linear alignment error signals used for the north end control.
These results show that the C6 sensitivity is limited below 30 Hz by angular control noises of the arm mirrors which are under local control. Nevertheless the mechanism which propagates these noises to the dark fringe signal has still to be understood. A possible scenario to explain a first order coupling between the angular noise of the mirrors and the dark fringe signal would be that the beam is miscentered with respect to the mirrors, as it has already been discussed for the beam splitter mirror in [1].

This analysis shows that other technical upgrades have to be planned in order to further reduce the mirror angular control noise:

- Some improvement is expected with the implementation of the full control bandwidth of the linear alignment for all the mirrors.
- A recentering of the mirrors with respect to the incident beam might reduce the coupling between the mirror angular motions and the dark fringe signal.

5.7 The C6 noise budget

The noise budget of the C6 run is shown in Figure 34. The incoherent sum of all the identified sources of noise explains reasonably well the sensitivity curve for all the Virgo bandwidth.
The low frequency part of the sensitivity curve is limited by several kinds of control noise: mirror angular control noise, mirror longitudinal control noise and actuator noise. The mirror angular control noises have a dominant impact for the frequencies below 30 Hz.

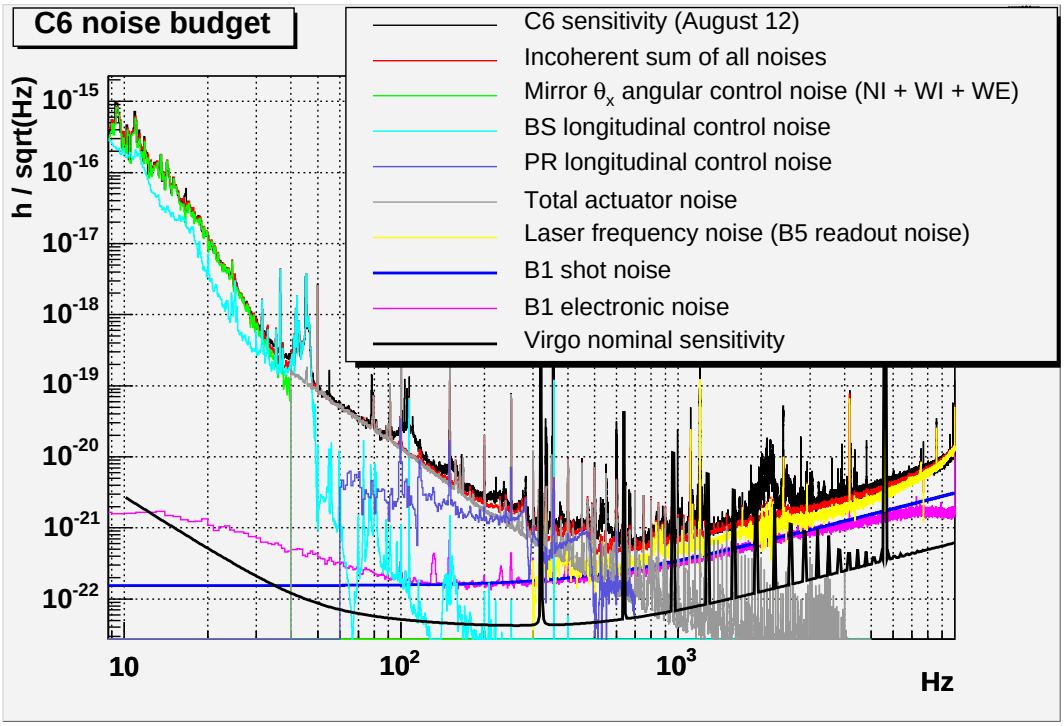

Figure 34: *Noise budget of the C6 run. The "mirror θ_x angular control noise" titled curve is the quadratic sum of the contributions of north input, west input and west end mirrors. For each mirror the contribution in sensitivity of the angular control noise has been estimated by using the coherence function between the corresponding correction signal and $B1\_ACp$. The contribution of the power recycling (PR) mirror longitudinal control noise has also been estimated from a coherence function, whereas the contribution of the beam splitter (BS) longitudinal control noise is obtained from the analytical model assuming a mistuning of* 55 % *of the α coefficient.*

The noise structures visible in the sensitivity curve between 30 and 50 Hz (identified as input bench resonances) are introduced by the beam splitter longitudinal control loop. The power recycling mirror control loop slightly contributes to the sensitivity in the region between 100 and 500 Hz. The actuator noise, which is dominated by a non linear noise, limits the sensitivity between 50 and 200 Hz.
For what concerns the intermediate frequencies, two sources of noise, identified at the beginning of the run, have been suppressed: These are the 70-500 Hz bump induced by spurious reflected beams, and the power noise which contributed to the sensitivity between 200 and 1000 Hz.
The high frequency part of the sensitivity (above 600 Hz) is limited by several sources of noise: the laser frequency noise (induced by the electronic noise and the shot noise of the $B5\_d1$ photodiode), the shot noise and the electronic noise of the B1 photodiodes. The noise structure visible in the sensitivity curve around 2kHz is due to the vibrations generated by the turbo pump of the detection tower.
The need for several technical upgrades has been pointed out by the analysis of the C6 sensitivity. Some of these upgrades, which were achieved during the four weeks between the C6 run and the C7 run, are presented in the next section.

6 Analysis of the C7 run sensitivity

This section is devoted to the analysis of the sensitivity obtained during the C7 run. This sensitivity has been significantly improved with respect to the C6 sensitivity (obtained one month before), especially in the low frequency region (below 500 Hz) as shown in Figure 2. The technical upgrades which allowed these improvements are described in the following.

6.1 Dark fringe readout noises and laser frequency noise

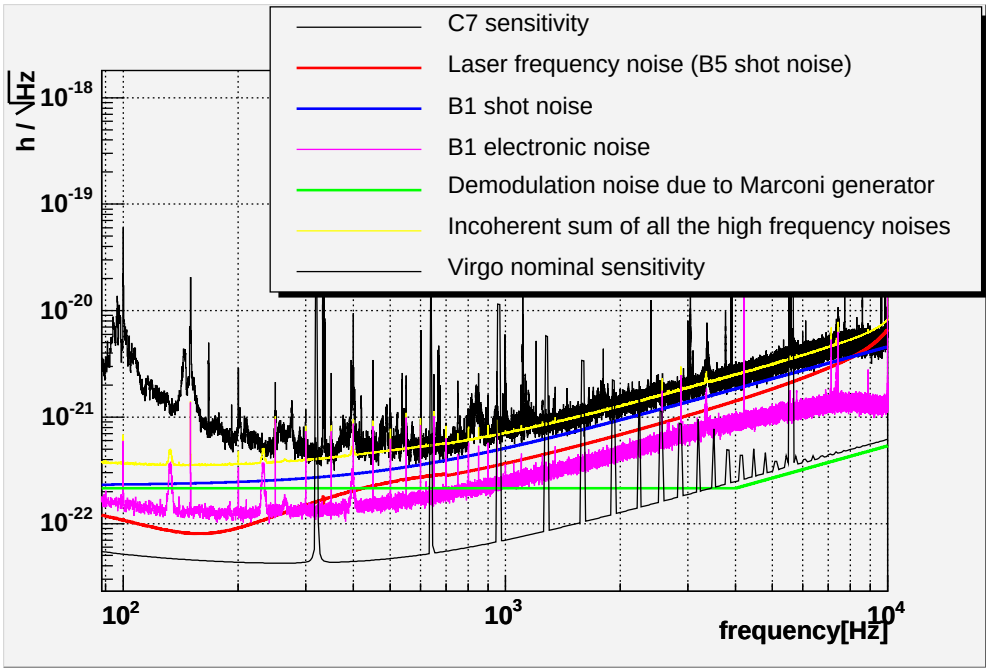

Figure 35: *Noises limiting the sensitivity at high frequency during the C7 run.*

During the C6 run, the sensitivity obtained at high frequency was limited by the readout noises (electronic noise and shot noise) of the B1 and B5 photodiodes, as shown in 5.1 and 5.3 respectively. Consequently, the two following upgrades have been performed in order to reduce the contribution of the high frequency noises before the C7 run:

- The optical setup of the B5 photodiode which provides the error signal of the laser frequency stabilization loop has been modified so that the power reaching this photodiode is multiplied by a factor 3. This upgrade results in an increase of the signal to noise ratio. Thus the impact of the B5 electronic noise is reduced by a factor 3 and the impact of the B5 shot noise by a factor $\sqrt{3}$. After this upgrade the B5 electronic noise becomes negligible with respect to the shot noise.

- The modulation index has been increased from 0.16 to 0.30, which increases the amplitude of the sidebands by about a factor 2. As a consequence, all the photodiode signals demodulated at the modulation frequency (the AC signals) are also amplified by a factor 2. The signal used for the control of the PR mirror (B2_3f_ACp) is

demodulated at three times the demodulation frequency and is therefore amplified by a factor $m^3 \approx 8$. The case of the DC signals depends on the beam which is considered. For the beams which do not result from a destructive interference the DC power is dominated by the carrier and is therefore unchanged by this modification. This is the case for B5. For beams which result from a destructive interference the DC power is dominated by the power of the sidebands and therefore varies with the square of the modulation depth. This is the case for B1 since the contrast defect is quite small ($1 - C \approx 5 \times 10^{-5}$).
Therefore the change of the modulation index results in a reduction by a factor 2 of the contribution in sensitivity of the B5 shot noise and the B1 electronic noise. On the contrary the contribution of the B1 shot noise is mainly unchanged: the shot noise at the output of this photodiode increases in the same way than the amplitude of the demodulated signal.

The upgrades previously mentioned should allow the reduction of the contribution in sensitivity of the B5 shot noise (which couples to the dark fringe signal through laser frequency noise), and the reduction of the contribution of B1 electronic noise. Nevertheless it has to be noticed that the contribution of the laser frequency noise in the dark fringe signal also depends on the CMRF which can vary with the alignment conditions. During the C7 run the alignment conditions were not so stable as during the C6 run due to a lack of time to test the robustness of the recent upgrades of the linear alignment, so that the CMRF was slightly worsened. This is the reason why the contribution of laser frequency noise to the C7 sensitivity (shown in Figure 35) is not reduced as expected with respect to the C6 run. However some changes in the relative contributions due to the technical upgrades can be noticed: The contribution of B5 shot noise is now slightly smaller (by 20 %) than the contribution of the B1 shot noise, and the contribution of the B1 electronic noise is reduced by a factor 2 with respect to the contribution of the shot noise.
The impact of the control noise of the power recycling control loop observed during C6 and discussed in 5.6.2 is reduced by about a factor 8 with the increase of the modulation depth and is no more visible during C7.
The contribution of the demodulation noise induced by the Marconi generator has been also included in Figure 35: It is comparable to the contribution of the B1 electronic noise at 1 kHz. The incoherent sum of all the noises identified at high frequency explains reasonably well the sensitivity floor between 300 Hz and 10 kHz.
The contributions of B1 and B5 shot noises shown in Figure 35 will be lowered by increasing the power resonating inside the recycling cavity. The contribution of the demodulation noise will be lowered by replacing the Marconi generator by the LNFS-100 (as mentioned in 5.1.1) and by improving the alignment conditions.

6.2 Environmental noise

During the C7 run, the dark fringe signal $B1\_ACp$ is coherent with several signals related to the injection system for the frequencies associated to the structures visible in the sensitivity curve between 400 Hz and 2 kHz. The left plot on Figure 36 shows the coherence obtained between $B1\_ACp$ and the error signal of the laser frequency stabilization loop ($B5\_ACp$), when all the vacuum pumps are running. This coherence indicates that the sensitivity might be limited in this frequency region by a laser frequency noise. The right

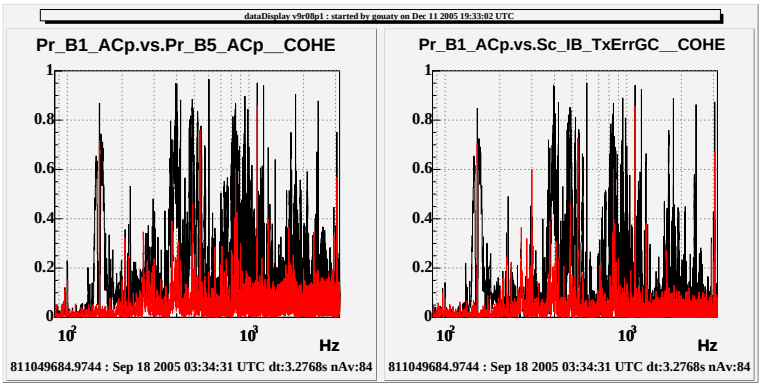

Figure 36: *Coherence function between the dark fringe signal (B1_ACp) and respectively: the error signal of the laser frequency stabilization loop (B5_ACp) on the left plot, the error signal of the θ_x angular control loop of the mode cleaner end mirror on the right plot. The black curves show the coherence obtained when the pumps are running, whereas the red curves show the coherence obtained when the input bench pumps are switched off.*

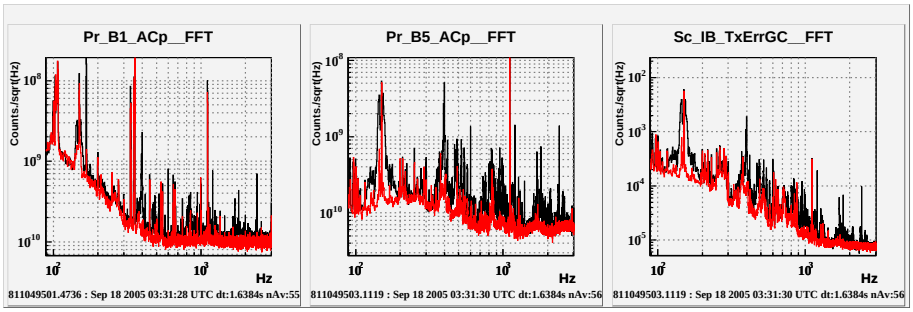

Figure 37: *Comparison between some spectra obtained with input bench pumps running (black curves) and with input bench pumps stopped (red curves). From left to right: dark fringe signal (B1_ACp), error signal of the laser frequency stabilization loop (B5_ACp), and error signal of the θ_x angular control loop of the mode cleaner end mirror.*

plot on Figure 36 shows that *B1_ACp* is also coherent with the error signal used to control the θ_x degree of freedom of the input mode cleaner end mirror, which shows that this noise enters the interferometer through the injection system. Then the origin of the noise could be explained by a scenario quite similar to that presented in 5.4.1: Some environmental noise in the laser laboratory might induce beam jitter which is converted into power noise or frequency noise at the exit of the input mode cleaner (IMC) cavity. As the power noise has been reduced during the C6 run (as shown in 5.4.1) and as no coherence is still visible between *B1_ACp* and the signal measuring the power transmitted by the IMC cavity, the hypothesis of frequency noise is favoured.

A test consisting in switching off all the vacuum pumps has been performed at the end of the C7 run in order to check if the pump operation generates noise in the sensitivity curve (as it was during the C6 run). The coherences shown in Figure 36 almost disappear when the input bench tower pumps are stopped. Moreover the noise structures visible in the dark fringe signal above 400 Hz are significantly reduced when the pumps are not

running, as shown in Figure 37. A similar behaviour can be noticed for what concerns the signals related to the injection system (the $B5\_ACp$ signal and the error signal of IMC end mirror angular control loop). These results prove that the noise structures observed in the sensitivity curve between 400 Hz and 2 kHz are correlated to the environmental noise generated by the pumps of the input bench tower. This noise may couple to the dark fringe signal through laser frequency noise. Several technical improvements can be planned in order to reduce the impact of environmental noise in the laser laboratory:

- The acoustic and seismic isolation of the optical input benches can be improved.
- The coupling between the beam jitter and the frequency noise obtained at the exit of the IMC cavity might be reduced with a better alignment of the incident beam with respect to the IMC.

6.3 Actuator noise

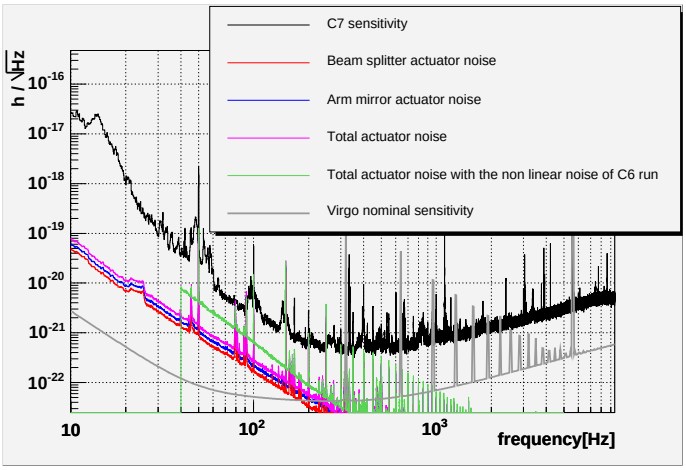

Figure 38: *Contribution in sensitivity of the actuator noise during the C7 run. These contributions are obtained from the standard estimation of the actuator noise (based on the measurement of the coil current when no correction signal is sent to the DAC) except for what concerns the top estimation (green curve): This one is obtained by assuming that the driven coils (four coils for the beam splitter and two coils for the north end mirror) are dominated by a non linear noise which is at the same level as that given by the measurement of August* 18^{th} *(used for the C6 run) in term of voltage at the DAC output.*

After the C6 run the hierarchical control has been implemented on the end arm towers which allowed the reduction of the dynamic range of the corrections applied to the end mirrors. This made it possible to increase the serial resistor R_{serie} up to 6 $k\Omega$ for the arm coils. This upgrade results in a reduction by a factor 23 of the standard arm actuator noise with respect to the C6 run. The serial resistor of the beam splitter coils has also been increased up to 1 $k\Omega$, which allowed the reduction by a factor 23.5 of the standard beam splitter actuator noise with respect to the C6 run.
The contribution in sensitivity of the standard actuator noise (without taking into account the non linear noise described in the analysis of the C6 run) is shown in Figure 38.

The estimation of the arm mirror actuator noise and the estimation of the beam splitter actuator noise have been obtained by using the relations (29) and (30) respectively, with $k_a \approx \frac{1}{550}$ for the arm mirrors and $k_a \approx \frac{1}{90}$ for the beam splitter. The conversion factor of the beam splitter has also been measured after these modifications with the same method as described in 4.3 and gives: $K_{DC} = 33 \pm 7\ \mu m/V$. As shown in Figure 38 the contribution of the standard actuator noise remains lower than the sensitivity by about a factor 10 in the region between 60 and 100 Hz. However the actuator noise of the driven coils is likely to be worsened by non linear noise, as it has been shown in 5.5.2.

The contribution of the non linear noise has been computed by assuming that its level expressed as an equivalent DAC output voltage (δu_{nl}) is the same as that measured for the C6 run (2400 $nV/\sqrt{Hz}$ at 50 Hz and 440 $nV/\sqrt{(Hz)}$ at 500 Hz). The contribution of the total actuator noise, including the non linear noise on the four beam splitter coils and on two coils of the north end mirror (during the C7 run no longitudinal correction was sent to the west end mirror) is shown in Figure 38. It remains about a factor 3 lower than the sensitivity curve. Nevertheless this estimation could be underestimated because the hypothesis according to which δu_{nl} would be the same for the two runs is questionable. Indeed, as explained in 5.5.2, the non linear noise increases when the amplitude of the correction signal sent to the DAC increases (but the relation between these two quantities has not been clearly established). During the C7 run higher corrections signals (about 5 times higher for the north end mirror) have to be sent to the DAC in order to compensate the increase of the serial resistor. Thus the effective contribution of the total actuator noise (with non linear noise) could be worse than the estimation shown in Figure 38. Nevertheless it is shown in 6.3.2 that the sensitivity is limited by other sources of noise between 60 and 100 Hz.
After the C7 run a retuning of the electronics of the actuator has been performed so that the non linear noise should be suppressed. The expected standard actuator noise is still a factor 5 to 10 higher than the Virgo nominal sensitivity as shown in Figure 38. Therefore it is also planned to add analogic filters inside the actuator chain in order to lower the contribution of actuator noise below the nominal sensitivity.

6.4 Noise introduced by the control loops

During the C7 run the low frequency part of the sensitivity (below 100 Hz) is limited by beam splitter longitudinal control noise (between 40 and 50 Hz) and by mirror angular control noises.

6.4.1 Noise introduced by the beam splitter longitudinal control loop

During C7 the α-technique described in 5.6.1 was also used and the value of α coefficient tuned at the beginning of the run. The contribution in sensitivity of the beam splitter longitudinal control noise has been estimated by using relations (33) and (34), assuming a mistuning of 7 % of the α coefficient (instead of 45 % for the C6 run). The result is shown in Figure 39. The model taking into account the α technique suits well to the structure at 42 Hz (identified as an input bench mechanical resonance) and to the struc-

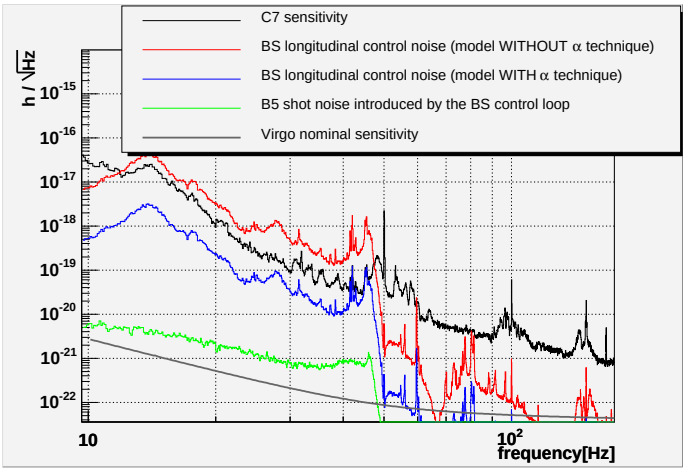

Figure 39: *Contribution of the beam splitter (BS) longitudinal control noise in the C7 sensitivity. The model taking into account the α technique is obtained with a α coefficient mistuned by 7 %.*

ture at 45 Hz (already mentionned in 5.6.1) visible in the sensitivity curve. The model of the beam splitter longitudinal control noise without the α technique is plotted for comparison. One can notice that the beam splitter longitudinal control noise is reduced by about a factor 14 with the α technique, whose efficiency has been increased with respect to the C6 run thanks to a better tuning of the α coefficient. This improvement is clearly seen on Figure 2 which compares C6 and C7 sensitivities. Nevertheless the C7 sensitivity is limited between 40 and 50 Hz by the beam splitter longitudinal control noise.

The origin of beam splitter control noise has been identified as the input bench resonances between 40 and 50 Hz. For what concerns the frequencies below 40 Hz, the origin of this noise has not been clearly identified. However a good coherence (up to 80 %) is observed in the region around 14 Hz between the BS longitudinal correction signal and several angular correction signals (the north end mirror θ_x correction, the north input mirror θ_y correction and the power recycling mirror θ_y correction). This means that some mirror angular control noise might couple to the error signal of the BS longitudinal control loop. A simulation study performed with SIESTA [2] indicates that the contribution of the B5 shot noise (which is higher than the B5 electronic noise during the C7 run) introduced by the beam splitter longitudinal control is negligible as shown in Figure 39.

6.4.2 Noise introduced by the angular control loops

Identification of the angular control loops introducing noise in the dark fringe signal

The dark fringe signal is coherent with several angular correction signals during the C7 run, as shown in Figure 40. The largest coherent functions are obtained with the corrections sent to the west input mirror (which is the only mirror still under local control), to the north input mirror and to the power recycling mirror. Some coherence has also been found with other correction signals (not shown in Figure 40) at very low frequency (below 20 Hz).

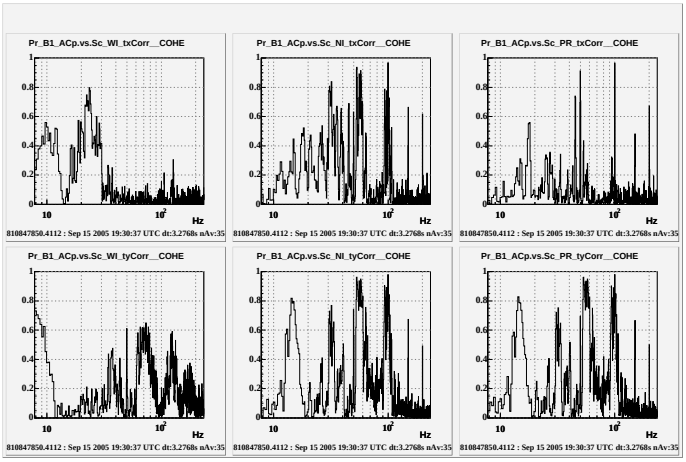

Figure 40: *Coherence functions obtained during the C7 run between the dark fringe signal and the following angular correction signals: the correction signals of the west input mirror (top left plot for θ_x and bottom left plot for θ_y), the correction signals of the north input mirror (top middle plot for θ_x and bottom middle plot for θ_y), and the correction signals of the power recycling mirror (top right plot for θ_x and bottom right plot for θ_y).*

One can notice that the coherence functions between the dark fringe signal and the θ_y correction signals sent respectively to the north input and to the power recycling mirrors are very similar (see the middle and right bottom plots of Figure 40). This is explained by the fact that both of these correction signals receive a contribution from the same quadrant photodiode (which is located on the north end optical bench). Moreover the noise is suspected to be introduced by the angular control loop of the north input mirror rather than the one of the power recycling (PR) mirror, because a motion of the PR mirror cannot directly produce a difference of length between the two arms. On the contrary, as it has been discussed in 5.6.3, a motion of the input mirrors can induce a difference of length between the two Fabry Perot cavities if the beam is miscentered with respect to this mirror. As a consequence, it is assumed in the following that the sensitivity is mainly limited by the noises introduced by the west input and north input mirrors.

Origin of the noise propagated by the angular control loops

The noise introduced by the west input angular correction signals most likely comes from the readout noise of the local control sensors.
The noise introduced by the north input angular correction signals cannot be explained so easily because this mirror is under linear alignment. However Figure 41 shows that these signals are coherent with the seismic noise measured in the north end building, near the optical bench where the quadrant photodiode contributing to the error signals of the north input angular control loops is located. This indicates that the environmental noise of the north end building propagates in the interferometer through the north input angular control loops. An hypothesis which could explain how environmental noise couples to the error signals of the quadrant photodiode would be the presence of spurious diffused beams in the north end optical bench (as it was already discovered during the C6 run).

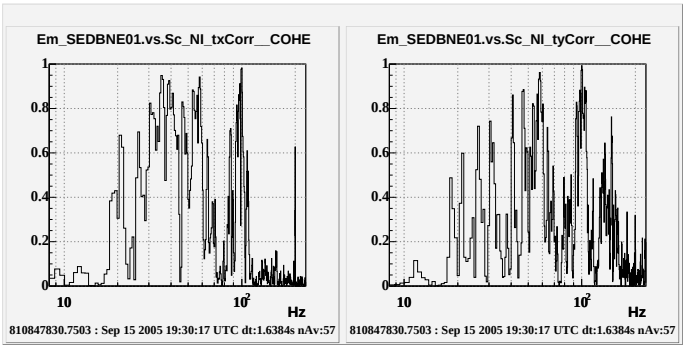

Figure 41: *Coherence functions obtained between the angular correction signals of the north input mirror and a seismic noise sensor located in the north end building.*

Contribution of the angular control noises in the C7 sensitivity

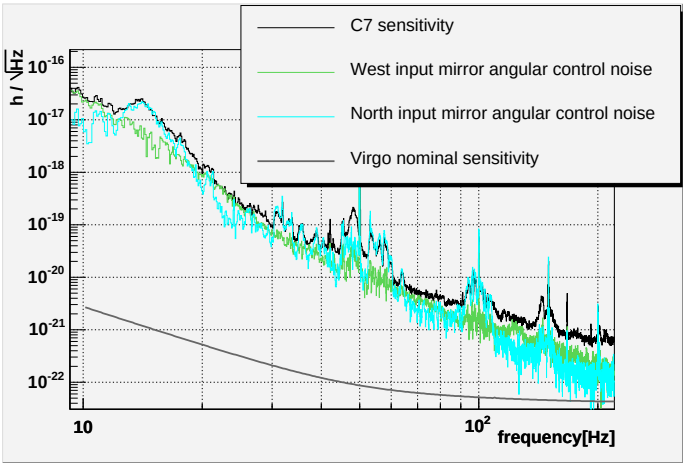

Figure 42: *Contributions in sensitivity of the west input and north input mirror angular control noises estimated from the coherence functions. For each mirror the contributions of both θ_x and θ_y angular control noises are quadratically summed. The validity of these estimations depends on the relevancy of the hypothesis according to which only these two angular control loops introduce noise in the sensitivity.*

The contributions in sensitivity of the west input and north input mirror angular control noises are shown in Figure 42. These contributions have been obtained from the coherence functions of Figure 40, assuming that only the west input and north imput angular control loops introduce noise. The north input angular control noise explains several structures visible in the sensitivity curve, in particular the noise structures between 50 and 60 Hz, and between 90 and 110 Hz. The west input angular control noise has a significant impact on the sensitivity from 10 Hz up to 135 Hz.

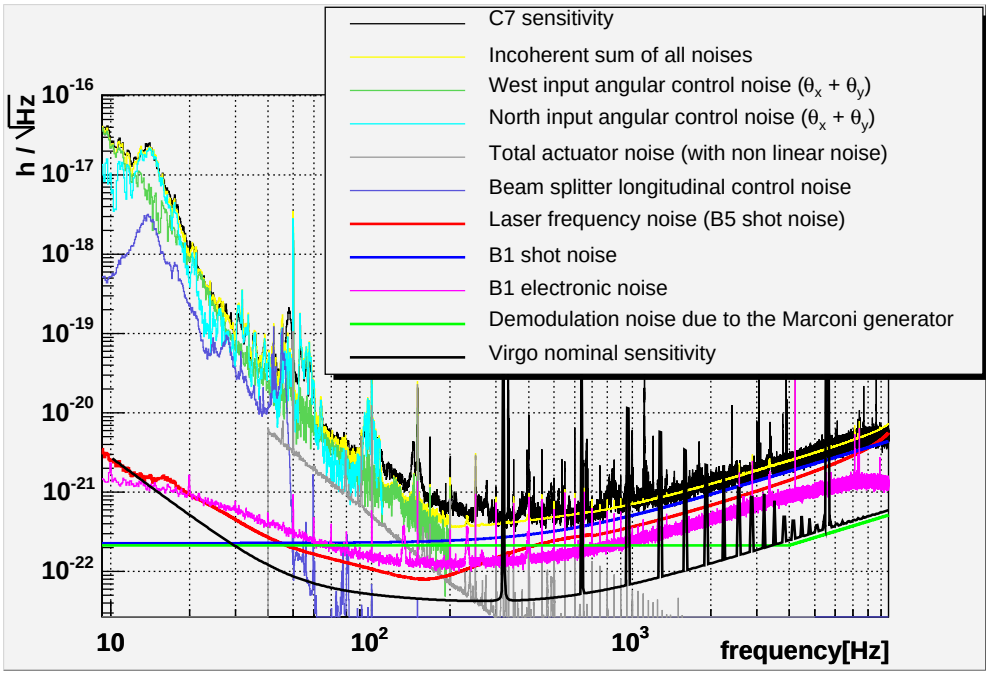

Figure 43: *Noise budget of the C7 run. The contributions of the west input and north input angular control noises have been estimated from the coherence functions between the angular correction signals and the dark fringe signal, assuming that only the west input and north input angular control loops introduce noise in the sensitivity. The beam splitter longitudinal control noise is obtained by assuming a mistuning of* 10 % *of the* α *coefficient. For what concerns the contribution of the actuator noise, the non linear noise is extrapolated from a measurement performed in the same conditions as the C6 run.*

6.5 The C7 noise budget

The main results of the analysis of the C7 run are summarized by the noise budget shown in Figure 43. The sensitivity is reasonably well explained at low frequency (up to 100 Hz) by the mirror longitudinal and angular control noises. At high frequency (above 300 Hz), the sensitivity floor is limited by the shot noise of the B1 and B5 photodiodes. Several noise structures visible above 400 Hz have been related to environmental noise inside the laser laboratory which couples to the dark fringe signal as a laser frequency noise. Between 100 and 300 Hz both control noises and photodiode readout noises contribute to the sensitivity curve, but the structure around 150 Hz is not understood.

7 Conclusion

Between C5 and C7 runs the sensitivity of the recycled interferometer has improved by one to more than two orders of magnitude, depending on the frequency range. These improvements are the result of technical upgrades which followed the identification of the sources of noises and their coupling mechanism to the dark fringe which have been presented in this note.

The low frequency region (below 100 Hz) was dominated by beam splitter longitudinal

and angular control noises during C5. Improvements of the filters used in these control loops allowed to reduce the impact of these noises on the sensitivity of C6. As a result the sensitivity is improved by more than a factor 10 between C5 and C6 runs. Noises arising from the local controls of the input mirrors appeared during C6 run. After C6, the implementation of the linear alignment on all mirrors except the west input allowed a further improvement of the sensitivity below 50 Hz. The implementation and the good tuning of the so-called α technique also helped in the reduction of the beam splitter longitudinal control noise. These resulted in a gain of about a factor 10 in sensitivity below 50 Hz. The implementation of the linear alignment as well as a better centering of the beam on the mirrors should allow further improvements in this frequency domain.

After the improvement of the filter used for the beam splitter longitudinal control it was possible to reach the noise of the mirror actuators above 50 Hz during C6. This noise was then reduced for the C7 run thanks to the implementation of the hierarchical control and a modification of the electronics of the actuation chain. The region around 100 Hz was then limited by both actuator noise and angular control noise during C7. Further improvements should be gained with the complete implementation of the linear alignment and upgrades of the actuators electronics.

In the intermediate frequency region (few hundred Hertz) the power recycling longitudinal control noise limited the C6 run sensitivity. This noise was reduced and no more visible during C7 thanks to the increase of the modulation index. In this frequency range there was also some structures originating from environmental noise in C6 and C7 sensitivities. During C6 it was found to be power noise originating from beam jitter on the input mode cleaner. An upgrade of the power stabilization allowed to get rid of this noise at the end of C6. Some laser frequency noise also probably originating from beam jitter was responsible for some structures during C7. This environmental noise is clearly generated by the vacuum turbo pump of the injection tower. The detection tower turbo pump was also found to be responsible for the 2 kHz structure present in C6 run. The coupling of these noises with the dark fringe should be reduced with a better alignment of the input beam on the input mode cleaner and a better isolation of the injection and detection optic benches.

In the high frequency region (above few hundred Hertz), the sensitivity was limited by demodulation noise during C5. This noise was originating from the phase noise of the local oscilator board which coupled to the dark fringe due to the bad alignment conditions. This noise has been reduced with the improvement of the LO board and its coupling to the dark fringe reduced thanks to the implementation of a simplified version of the linear alignment (the drift control). The phase noise was therefore reduced by almost two orders of magnitude between the C5 and C6 runs. It was then found that C6 sensitivity was limited by laser frequency noise. This noise was originating from the readout noise of the photodiode (B5) used for the frequency stabilization. A reduction of this readout noise and an increase of the modulation depth led to a reduction of this noise below the dark fringe shot noise. The C7 sensitivity is therefore limited by the shot noise of the dark fringe and of the B5 photodiode. The sensitivity will therefore be improved with the increase of the power incident on the beam splitter which will result from the installation of the new input bench and the new power recycling mirror.

References

[1] R. Flaminio, R. Gouaty, E. Tournefier, *Analysis of the sensitivity of the recombined interferometer during C4 and C5 runs.*, Note Virgo VIR-NOT-LAP-1390-312 (2006).

[2] B. Caron et al., A time domain, general purpose simulation program for the VIRGO experiment, Astropart. Phys., 10/4, 369-386 (1999).

[3] M. Barsuglia, *Stabilisation en fréquence du laser et contrôle de cavités optiques à miroirs suspendus pour le détecteur interférométrique d'ondes gravitationnelles VIRGO.*, Ph. D. thesis, University of Orsay (1999).

[4] F. Beauville, *Prélude à l'analyse des données du détecteur Virgo : De l'étalonnage à la recherche de coalescences binaires.*, Ph. D. thesis, University of Savoie (2005).

[5] M. Laval, F. Bondu, JY. Vinet, *Optical simulation, mirror curvatures and long arms*, Virgo Note VIR-NOT-OCA-1390-300 (2005).

A Coupling of phase noise in the dark fringe signal

The interferometer signal (S_{ITF}) reaching the B1 photodiodes can be described as the sum of in-phase and in-quadrature components:

$$S_{ITF} \;=\; S_p cos\Big(2\pi\nu_{mod}t + \delta\phi_{ITF}(t)\Big) \;+\; S_q sin\Big(2\pi\nu_{mod}t + \delta\phi_{ITF}(t)\Big) \tag{35}$$

where S_p is the amplitude of the in-phase component (induced by a difference of length between the two Fabry Perot cavities), S_q is the amplitude of the in-quadrature component (induced by mirror misalignments), ν_{mod} is the modulation frequency, and $\delta\phi_{ITF}(t)$ is the phase fluctuation of the interferometer signal.
The signal S_{dem} obtained after the demodulation process in the ACp channel is given by:

$$S_{dem} \;=\; S_{ITF}.S_{LO} \tag{36}$$

where S_{LO} is the local oscillator signal:

$$S_{LO} \;=\; cos\Big(2\pi\nu_{mod}t + \delta\phi_{LO}(t)\Big) \tag{37}$$

$\delta\phi_{LO}(t)$ is the phase fluctuation of the oscillator signal.
By developing relation (36) one obtains:

$$\begin{aligned} S_{dem} \;=\; & \frac{S_p}{2}\Big(cos(4\pi\nu_{mod}t + \delta\phi_{ITF}(t) + \delta\phi_{LO}(t)) \;+\; cos(\delta\phi_{ITF}(t) - \delta\phi_{LO}(t))\Big) \\ & + \frac{S_q}{2}\Big(sin(4\pi\nu_{mod}t + \delta\phi_{ITF}(t) + \delta\phi_{LO}(t)) \;+\; sin(\delta\phi_{ITF}(t) - \delta\phi_{LO}(t))\Big) \end{aligned} \tag{38}$$

In relation (38) the components at twice the modulation frequency are suppressed by the detection electronics. Finally the $B1\_ACp$ signal obtained at the output of the detection chain is given at the first order approximation by:

$$B1\_ACp \;=\; \frac{S_p}{2} \;+\; \frac{S_q}{2}\delta\phi_{dem}(t) \tag{39}$$

where $\delta\phi_{dem}(t)$ is the relative fluctuation of phase between the interferometer signal and the local oscillator signal: $\delta\phi_{dem}(t) = \delta\phi_{ITF}(t) - \delta\phi_{LO}(t)$.
Relation (39) can also be written as:

$$B1\_ACp = ACp_0 + \delta ACp \tag{40}$$

where:

- $ACp_0 = \frac{S_p}{2}$ is the DC signal induced by a difference of length between the two arms.
- $\delta ACp = \frac{S_q}{2}\delta\phi_{dem}(t) = ACq_0.\delta\phi_{dem}(t)$ is the contribution of the phase noise to the dark fringe signal, it is proportional to the amount of signal seen in the ACq channel.

The previous computation shows that a relative fluctuation of phase between the interferometer signal and the local oscillator signal used for demodulation generates a noise in the dark fringe signal given in the frequency domain by:

$$\delta\tilde{ACp} = ACq_0.\delta\tilde{\phi}_{dem} \tag{41}$$